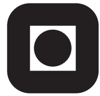

NTNU – Trondheim
Norwegian University of
Science and Technology

Refining of Silicon by Solidification of Al-Si Melt

Sissel Richardsen

Chemical Engineering and Biotechnology
Submission date: June 2012
Supervisor: Merete Tangstad, IMTE

Norwegian University of Science and Technology
Department of Materials Science and Engineering

I hereby declare that this work has been carried out independently and in compliance with the examination regulations of the Norwegian University of Science and Technology, NTNU.

Sissel Richardsen

Trondheim, June 2012

Preface

This thesis describes the growth of primary Si crystals from an Al-Si melt, which is a refining method to obtain SoG-Si. The work is the master thesis of the author, and a basis for evaluation of the course TMT 4900 at the Norwegian University of Science and Technology, NTNU. The work has been based on a collaboration between NTNU and Clean Silicon AS, and was part of the BASIC project.

First of all I would like to thank my supervisor, Professor Merete Tangstad, for giving me the opportunity to work with such an interesting subject and for great guidance and instructive input throughout this work. Merete has also given me the opportunity to attend several conferences, both in Norway and USA, during the final year of my master degree.

I am very grateful for my co-supervisor Dr. Harsharn Tathgar at Clean Silicon AS, for helpful input on experimental work and for providing material. I would like to express my sincere gratitude to Antoine Autruffe for all his help with the resistance furnace and SEM operation. I would also like to thank Jafar Safarian for helping me with the induction furnace, Morten Raanes for help with the EPMA analyses and Syverin Lierhagen for help with the ICP-MS analyses.

Finally, a warm thank to Ines Sulentic for all help and for proof-reading this master thesis.

Abstract

Primary silicon crystals grown from an Al-Si melt has been investigated by solidifying directionally and under electromagnetic field. The goal of this thesis was to increase the size of the primary Si crystals and to agglomerate the crystals to one part of the melt. If achieved, this could simplify the following acid leaching process that is necessary to collect the crystals from the melt.

Seven experiments were conducted in a resistance furnace with directional solidification to investigate the agglomeration and size of the Si crystals. A mono-crystalline Si seed was added to the Al-Si melt in three of these experiments as an attempt to increase the crystal growth. The impact of stirring in the melt before solidification was investigated. Al-Si melt was directionally solidified without the aid of seed in three experiments. The silicon content in the alloy and pulling rate during solidification was varied in these experiments to find the appropriate Si crystal growth conditions. The growth of silicon crystals from a mono-crystalline Si seed without aluminium was performed to investigate the impact aluminium had on the seeded growth.

One experiment was conducted in an induction furnace to investigate the influence electromagnetic force has on the agglomeration of primary Si crystals.

Agglomeration of Si primary crystals was found not to be successful for either directional solidification or electromagnetic force method, as the crystals were not gathered to one part of the melt. The size of the primary Si crystals was not as large as expected and addition of mono-crystalline Si seed did not improve the crystal size.

A single Si crystal was successfully grown from a mono-crystalline Si seed when there was no aluminium in the melt.

Sammendrag

Vekst av primære silisium krystaller fra en Al-Si legering har blitt undersøkt ved rettet størkning og størkning under elektromagnetisk felt. Målet med denne oppgaven var å øke størrelsen på de primære Si krystallene og å agglomerere krystallene til en del av smelten.

Syv forsøk ble gjennomført i en resistansovn ved rettet størkning for å undersøke agglomerering og størrelse på Si krystallene. En énkrystall av Si har blitt tilsatt Al-Si legeringen i tre av disse forsøkene som et forsøk på å øke krystall veksten. Påvirkningen av røring i smelten før størkning har blitt undersøkt. Rettet størkning av Al-Si legeringen uten énkrystall ble undersøkt i tre forsøk. Silisium innholdet i legeringen og trekkhastigheten under størkning ble variert i disse forsøkene for å finne passende vekst forhold til Si krystallene. Vekst av Si krystaller fra en ènkrystall uten aluminium ble også utført for å undersøke hvilken påvirkning aluminium har på veksten.

Ett forsøk ble utført i en induksjonsovn for å undersøke hvilken påvirkning et elektromagnetisk felt har på agglomereringen av primære Si krystaller.

Det ble funnet at agglomerering av primære Si krystaller ikke var suksessfull for verken rettet størkning eller elektromagnetisk felt metoden, siden krystallene ikke ble samlet til en del av smelten. Størrelsen på de primære Si krystallene var ikke så store som forventet og tilsats av énkrystall forbedret ikke krystall størrelsen.

En enkelt silisiumkrystall vokste vellykket fra en énkrystall da det ikke var aluminium tilstede.

Table of Contents

Preface ..... **ii**

Abstract ..... **iii**

Sammendrag ..... **iv**

Table of Contents ..... **v**

1 Introduction **1**

2 Theory and literature **4**

2.1 Solvent material *4*

2.1.1 Requirements of the solvent 4

2.1.2 Solid solubility of aluminium 5

2.1.3 Solar cell efficiency 6

2.1.4 Aluminium content vs growth rate 7

2.2 Growth of silicon crystals *8*

2.2.1 Nucleation 8

2.2.2 Growth of silicon crystals in Al-Si alloys 12

2.2.3 Growth by directional solidification 15

2.2.4 The solid-liquid interface 17

2.2.5 Seeded growth of silicon crystals 21

2.3 Refining of silicon in Al-Si melt *22*

2.3.1 Segregation ratio of impurities 22

2.3.2 Refining by directional solidification 27

2.4 Acid leaching *30*

2.5 Electromagnetic separation *31*

3 Experimental work **36**

3.1 Overview of experiments *36*

3.2 Equipment *37*

3.2.1 Resistance furnace 37

3.2.2 Induction furnace 39

3.3 Materials *40*

3.3.1 DS experiments 42

3.3.2 SG experiments 43

3.3.3 SGS experiment 45

3.3.4 IH experiment 45

3.3.5 Silicon crystals 46

3.4 Analysing techniques *47*

3.4.1 Mechanical preparation of the samples 47

3.4.2 Analysis of silicon crystals by light microscopy 47

3.4.3 Electron probe micro-analyser (EPMA) 48

3.4.4 Electron backscatter diffraction (EBSD) 48

4 Results **49**

4.1 Position and size of primary Si crystals in DS and SG experiments *49*

4.2 Aluminium contamination in seed and primary Si crystals *52*

4.3 Position of Si primary crystals after electromagnetic separation *53*

4.4 Si crystal growth from seed without aluminium *55*

5 Discussion **57**

5.1 Analysis of the 35wt%Si master alloy *57*

5.2 Pulling rate during directional solidification *58*

5.3 Growth rate of Si crystals ... *61*
5.4 Positioning and size of the primary Si crystals by directional solidification ... *62*
5.4.1 Effect of temperature gradient and cooling rate ... 62
5.4.2 Si crystal area in cross-section compared to theoretical calculations ... 65
5.4.3 Morphology of Si crystals ... 65
5.4.4 Pulling rate and silicon content ... 66
5.4.5 Position of Si primary crystals by directional solidification ... 66
5.4.6 Length of primary Si crystals ... 69
5.5 Seeded growth ... *71*
5.6 EPMA analyses ... *72*
5.7 Electromagnetic separation ... *75*
5.8 Analysing technique ... *76*
6 Conclusion ... 78
7 Further work ... 80
References ... 81
Appendix 1 ... I
Appendix 2 ... II
Appendix 3 ... IV

1 Introduction

The growing demand for clean energy has opened up the market for solar cells. The worldwide production of photovoltaic modules is projected to approach 18 GW annually by 2020 from a production level of 1787 MW in 2005. [1] Crystalline silicon is the dominating feedstock for solar cells and had a market share of 91% in 2005. [2] Since silicon accounts for approximately 25 – 50 % or more (depending on the technology and the type of silicon used) of the cost of processed solar cells, it is necessary to develop a low cost silicon feedstock to supply the growing PV industry as the availability of suitable silicon feedstock is limited. [3]

Purification of metallurgical grade silicon (MG-Si) to solar grade silicon (SoG-Si), which is known as the metallurgical route, is one approach to obtain a low cost silicon feedstock for solar cells. [4] This route can be five times more energy efficient compared to the conventional Siemens process, [5] and several companies (Elkem, Heliotronic/Wacker, Bayer AG, Kawasaki Steel) have activities around development and production of low cost SoG-Si by this route. [4] However, to achieve the required purity for SoG-Si these companies have combined different purification steps (acid leaching, slag extraction, vacuum treatment, reactive gas blowing, directional solidification) in order to obtain SoG-Si from MG-Si. [4]

Clean Silicon AS is a company founded by Dr. Harsharn Tathgar. They are in the early stages to industrialise a purification technique where solvent refining is used to obtain SoG-Si from MG-Si. The keys of the method are to melt silicon under low temperature with aluminium as solvent and grow purified silicon crystals from the alloy melt as the impurities are segregated to the liquid alloy.

From pilot scale experiments they have obtained satisfactory results with this low energy refining technique, which gives a high yield of more than 95%. Figure 1.1 shows a flow sheet of this process. [6]

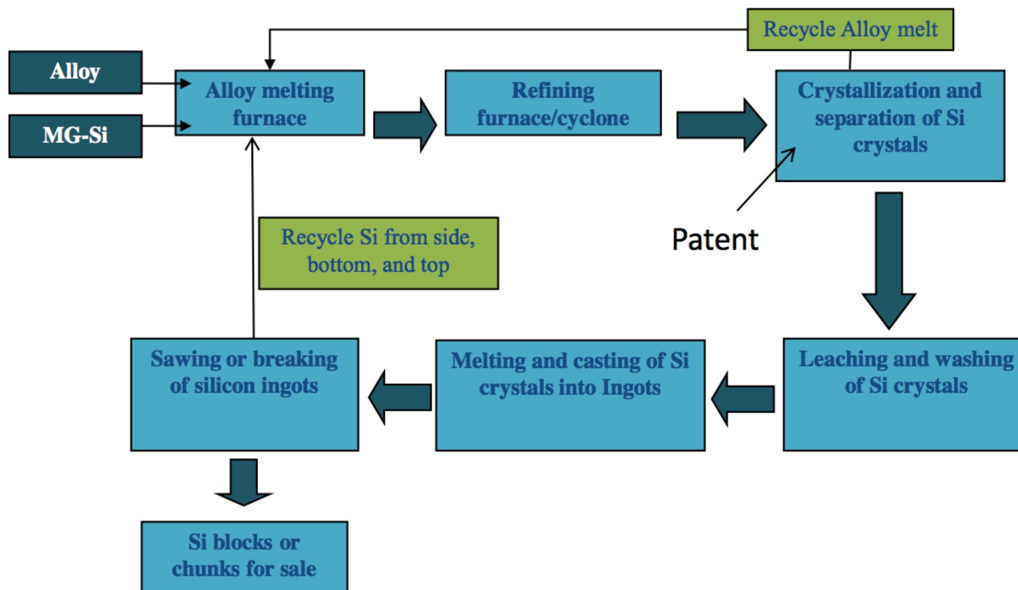

Figure 1.1, Flow sheet of process developed by Clean Silicon AS. [6]

Aluminium and MG-Si is alloyed at a temperature above 700°C and the silicon precipitates out as the melt is cooled down. The company has patented a technique for the crystallisation of silicon crystals in the melt. They have developed a unique method for the separation of Si crystals. After separation the silicon crystals will be covered by an aluminium layer, which is removed by acid leaching. It should be noted that the acid leaching would be more effective if the silicon crystals were larger in size. Since the aluminium lowers the melting point of the silicon, the energy consumption is only 20 kWh/kg, which may cut the electricity cost with 90% compared to current processes. Cut-off from casted ingots, the residue from wafer sawing and the alloy melt can be recycled, which makes the process even more energy efficient. [6]

This process does not need to be combined with other purification steps, as for several other companies, since the purification with solvent refining meets the demands for SoG-Si. This leads to faster building of the plant and more cost effective production as the time to market factor is reduced. The refined silicon is pure enough to qualify for both multi- and mono-crystalline solar cells and the

high purity implies that the solar grade silicon produced in this process will reach 90% of the market. [6]

In this work, the goal was to agglomerate silicon crystals in an Al-Si melt and obtain larger sized crystals during crystallisation by directional solidification and induced electromagnetic field. If this is achieved, the following leaching process could be simplified.

Directional solidification was expected to gather the silicon crystals in the lower part of the melt as the samples was pulled downwards in the furnace. Experiments with varying silicon content of the Al-Si alloy and pulling rates during directional solidification were conducted to investigate the impact these variables had on the silicon crystal growth from the melt together with the agglomeration of the crystals. These experiments are named the directional solidification (DS) experiments and the findings were used further during directional solidification with seeded crystal growth. Mono-crystalline silicon with a specific orientation was used as the seed and the silicon crystal growth was expected to increase in these experiments named seeded growth (SG) experiments. To determine whether it was possible to obtain silicon crystal growth from a seed with a given orientation, seeded growth with silicon (SGS) experiment was performed with directional solidification.

To investigate the silicon crystal growth and agglomeration of crystals by electromagnetic separation, an induction heating (IH) experiment was conducted. It was expected that the electromagnetic field would agglomerate the silicon crystals to one part of the melt.

This work was conducted under the BASIC research group at NTNU and in collaboration with Clean Silicon AS. The work presented in this thesis is done in order to start the solvent refining research in the BASIC group, as this is the first project regarding refining of silicon by solidification of Al-Si melt.

2 Theory and literature

Several metals can be alloyed with silicon for solvent refining at low temperatures. Selection criteria for the solvent and evaluation of aluminium as solvent material will be presented in this section. As the silicon is dissolved into the molten aluminium it melts down at a temperature much lower than the melting point of silicon. When the melt is cooled down silicon starts to grow in the melt and this is explained in the next part of this section.

The production of SoG-Si from MG-Si by solvent refining with Al-Si melt is a method for removing impurities at low temperature. [7] This refining effect is presented based on the literature and theory found on this topic. Agglomeration of silicon crystals by directional solidification and electromagnetic separation are treated separately. Acid leaching is necessary to remove the aluminium from the crystals and its effect on removal of impurities will be presented.

2.1 Solvent material

The choice of solvent material to dissolve silicon for solvent refining is crucial for the refining effect. In turn the refining effect determines the efficiency of the solar cell.

2.1.1 Requirements of the solvent

When alloying silicon with a solvent for refining of silicon there are five criterias that must be taken into account regarding the choice of solvent for this to be a efficient low-temperature process: [8]

1. No intermediate compound generated between solvent and silicon,
2. Low concentration of silicon, and low temperature, at the eutectic point,
3. Small segregation ratio of impurities between silicon and solvent,
4. High solubility of silicon in solvent at low temperature,
5. Easy separation of silicon crystals from the alloy.

Many metals can dissolve silicon at low temperature, but based on the criteria listed above, only aluminium, tin, zinc and indium are competent for solvent refining. Zinc has a low boiling point of 906°C, which would result in a serious loss of zinc. Indium is also not an option due to the high market price. According to Zhao and co-workers, [8] tin is the optimum solvent due to great density differences between the melt and the crystals together with large growth of the silicon crystals. However, the phase diagram of the Sn-Si system reveals that addition of silicon increases the melting temperature significantly. A small addition of 10wt% silicon will give a melting point of 1250°C, which is not much lower than the melting point of silicon. Therefore, tin does not qualify as a solvent for a low-temperature Si purification process if compared with the Al-Si system.

As a solvent, aluminium meets several of these criterias. The silicon solubility is high and the purification efficiency is high. [8] However, the density difference between silicon crystals and melt are low. The density of silicon crystals is 2330 kg/m^3 while the melt have a more or less constant density of 2430 kg/m^3 when following the liquidus line in the Al-Si phase diagram (see Figure 2.13). [9] It is therefor hard to separate the silicon crystals from the melt without acquiring a large cover of aluminium at the crystal surface. [8]

2.1.2 Solid solubility of aluminium

The solid solubility of aluminium in silicon is an important factor to the purification of silicon when aluminium is used as solvent. Concentration of aluminium in silicon at different temperatures were found by Yoshikawa and Morita [10] by EPMA measurements, seen in Figure 2.1. They found a maximum solid solubility of 430ppm around 1170°C.

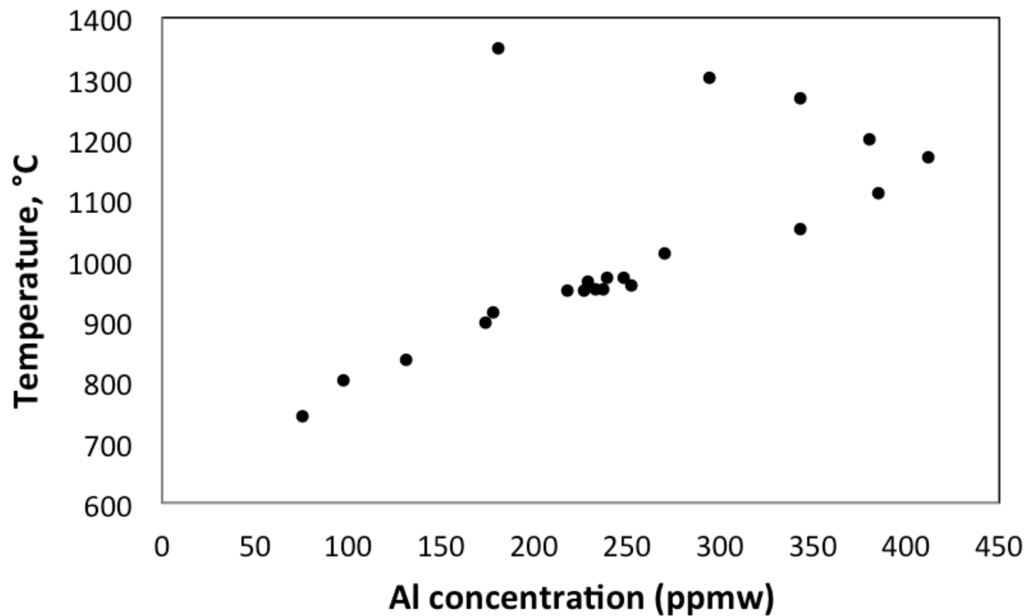

Figure 2.1, Solid solubilities of aluminium in silicon. Plotted from [10]

Murray and McAlister [11] found the maximum solubility of Al in Si at 1190°C, which is the retrograde point of the silicon solidus, to be 0,016 ± 0,003at%. Reported maximum solubilities are inconsistent with each other. However, the solid solubility of aluminium in silicon is higher than what is acceptable for SoG-Si feedstock, even at low temperature, and must be removed during solidification. It should be noted that the solid solubility decreases with decreasing temperature at temperatures lower than 1170°C - 1190°C, which means that the solvent refining with Al-Si melt at low temperature is promising in this respect.

2.1.3 Solar cell efficiency

6N Silicon Inc., Umoe Solar AS and International Solar Energy Research Center [12] purified MG-Si by solvent refining with aluminium. They obtained a 6N (99,9999%) purified material where the aluminium content observed was lower than 0,05ppmw. This content is much lower than the solid solubility and indicates that a further purification step is used, e.g. directional solidification. In addition they investigated the solar cell efficiency based on the refined 6N material. The average efficiencies exceeded 16%. Reference wafers based on

polysilicon were used to control the quality of the process. The same average efficiencies were obtained for both 6N material and polysilicon.

2.1.4 Aluminium content vs growth rate

Nishi and co-workers [7] investigated the aluminium content in samples solidified directionally with different crystal growth rates as shown in Figure 2.2. The aluminium content decreases with decreasing crystal growth rate. The aluminium content is higher than the solid solubility at 1000°C for most growth rates and indicates a possible entrapment of Al-Si melt in the silicon crystals. This can be prevented by controlling the growth rate, as explained in Section 2.2.2.

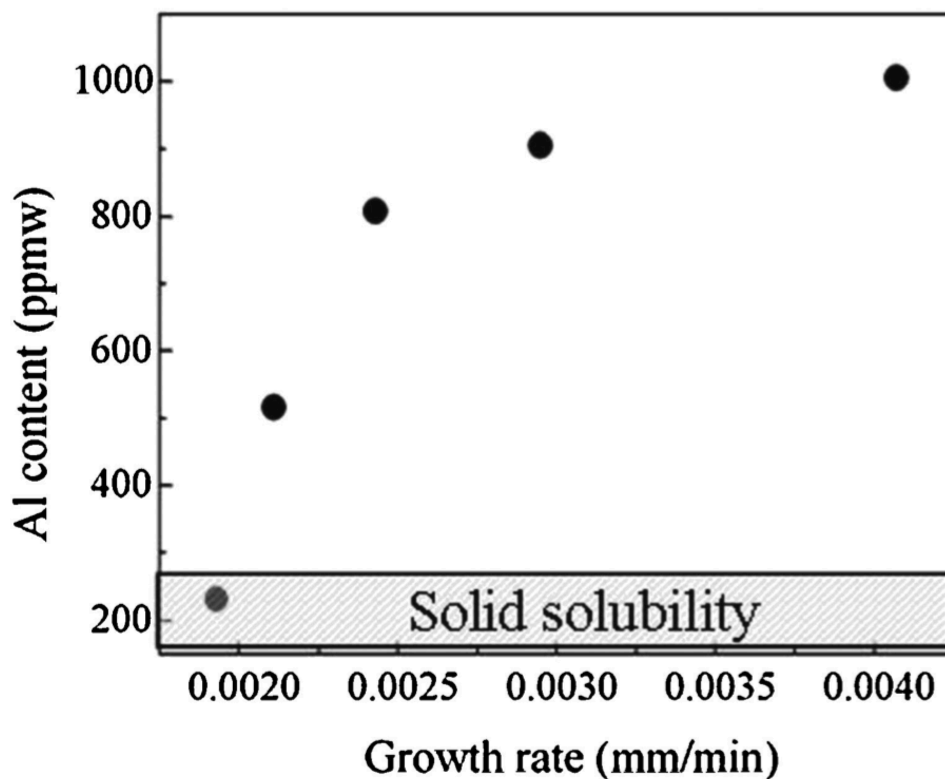

Figure 2.2, Relationship between aluminium content and growth rate of silicon crystals. The solidification temperature ranged from 900°C-1000°C. [7]

2.2 Growth of silicon crystals

It is important to mention nucleation and silicon crystal growth as they can influence the refining efficiency.

Most liquids solidify by crystallisation, which is the formation of solid crystals from a liquid. In order for crystals to develop there must exist a number of minute solid bodies, embryos, nuclei or seeds in the solution that act as centres of crystallisation. Thus, it can be said that crystallisation consists of two major events, nucleation and crystal growth. [13]

2.2.1 Nucleation

During a solidification process, heat is extracted from the melt. This heat extraction changes the energy of the solid and liquid phases in two ways. Due to cooling there will be an decrease in enthalpy of the liquid or solid, given by: $\Delta H = \int cdT$, and a decrease in enthalpy equal to the latent heat of fusion, ΔH_f, due to the transformation from liquid to solid. A heat flux from the system to the surroundings is required for solidification, which changes the free energy [14] and is considered as follows.

The change in the free energy is the driving force of any phase transformation including solidification, which is a liquid-to-solid phase transformation. [15] The nucleation of a crystal from its melt depends mainly on two processes: thermal fluctuations that lead to the creation of variously sized crystal clusters, and creation of an interface between the liquid and the solid. [14] The volume excess free energy change, ΔG_V, is associated with the creation of embryos and thereby proportional to the volume transformed. That is, proportional to the cube of the cluster radius, r^3. ΔG_V is a negative quantity below the equilibrium melting point, i.e. when the melt is undercooled, see Figure 2.3. The surface excess free energy change, ΔG_S, is associated with the creation of the interface and proportional to the area of solid/liquid interface formed. Thus, proportional to the square of the cluster radius, r^2, and is a positive quantity regardless of temperature. [13]

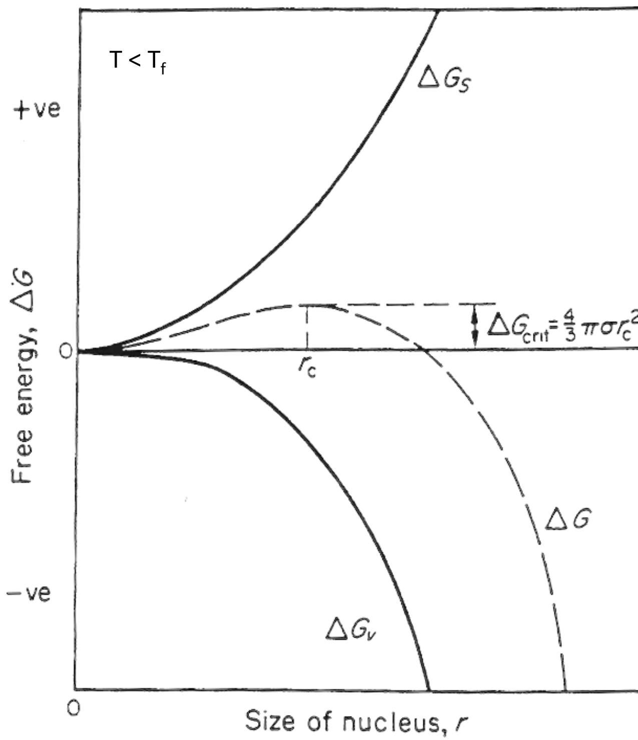

Figure 2.3, Free energy diagram for nucleation explaining the existence of a critical nucleus at temperatures, T, lower than the melting point, T_f. Modified from [13]

The overall excess free energy, ΔG, is equal to the sum of volume and surface excess free energy given in Equation 2.1.

$$\Delta G = \Delta G_S + \Delta G_V = 4\pi r^2 \gamma + \frac{4}{3}\pi r^3 \Delta G_v \quad (2.1)$$

Where γ is the interfacial tension and ΔG_v is the free energy change of the transformation per unit volume, v_m, and is proportional to the undercooling, ΔT, given in Equation 2.2. [13, 14]

$$\Delta G_v = \frac{\Delta G_V}{v_m} = -\Delta s_f \Delta T \quad (2.2)$$

Where Δs_f is the entropy of fusion per unit volume. If there is no undercooling, i.e. ΔT = 0, $\Delta G_V = 0$ and there will be no transformation, meaning that

undercooling is necessary for solidification to occur. [15] Metals and most other liquids are rarely undercooled by more than a few degrees before they begin to crystallise. [16]

At small values of the radius, the absolute value of ΔG_V is less than that of ΔG_S, while at large radius values the cubic dependence of ΔG_V predominates. Since the volume and surface excess free energy depend differently on the radius, the free energy of formation value passes through a maximum at a critical radius, r_C, which represents the minimum size of a stable nucleus. The maximum value, ΔG_{crit}, is found by maximizing Equation 2.1, setting $d\Delta G/dr = 0$.

$$\frac{d\Delta G}{dr} = 8\pi r\gamma + 4\pi r^2 \Delta G_v = 0 \qquad (2.3)$$

Therefor

$$r_C = \frac{-2\gamma}{\Delta G_v} \qquad (2.4)$$

Where ΔG_v is a negative quantity. From Equations 2.1 and 2.4 we get

$$\Delta G_{crit} = \frac{16\pi\gamma^3}{3(\Delta G_v)^2} = \frac{4\pi\gamma r_C^2}{3} \qquad (2.5)$$

When a cluster becomes larger than r_C, growth will occur due to the resultant decrease in the total free energy. [13, 14]

The nucleation described above is the process of homogeneous nucleation, where a solid forms within its own melt without the aid of foreign materials. [16] However, nucleation in solids is almost always heterogeneous, which is based on the assumption that the nucleation occurring on solid substrates foreign to the solidifying metal (e.g. at crucible wall, oxide layer, impurities, dislocations, inclusions etc.) all of which increase the free energy of the material. [17]

If a foreign substrate can induce nucleation at degrees of undercooling lower than those required for spontaneous nucleation, the overall free energy change associated with the formation of a critical nucleus under heterogeneous conditions $\Delta G'_{crit}$, must be less than the corresponding free energy change, ΔG_{crit}, associated with homogeneous nucleation, given by Equation 2.6. [13, 14]

$$\Delta G'_{crit} = \Delta G_{crit} f(\theta) \tag{2.6}$$

Interfacial tension, γ, is one of the important factors controlling the nucleation process. An interfacial energy diagram for three phases in contact is shown in Figure 2.4. $\gamma_{cl}, \gamma_{sl}, \gamma_{cs}$ are the interfacial tensions of cluster-liquid, substrate-liquid and cluster-substrate, respectively. The angle θ corresponds to the angle of wetting in liquid-solid systems. [13]

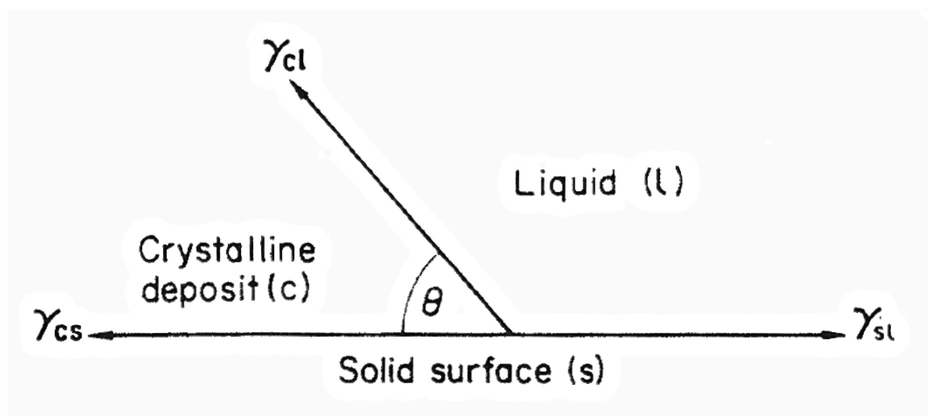

Figure 2.4, Interfacial tensions at the boundaries between three phases. [13]

The factor $f(\theta)$ is less than unity, and given by Equation 2.7. [14]

$$f(\theta) = \frac{(2 + cos\theta)(1 - cos\theta)^2}{4} \tag{2.7}$$

Where $\cos\theta$ is given by Equation 2.8. [13]

$$\cos\theta = \frac{\gamma_{sl} - \gamma_{cs}}{\gamma_{cl}} \tag{2.8}$$

If there is complete wetting θ = 0° there is no nucleation barrier, while θ = 180° correspond to homogeneous nucleation. All angles in between correspond to heterogeneous nucleation. [14]

Until now, the focus has been on primary nucleation. Secondary nucleation is when crystals of the solute are already present or deliberately added, so that the solution nucleates much more readily, [13] since the crystals have a catalysing effect on the nucleation. [18] There are several factors influencing secondary nucleation, and still the critical parameter is the degree of undercooling which control the rate of nucleation. A higher undercooling gives a larger number of nuclei. [18]

2.2.2 Growth of silicon crystals in Al-Si alloys

As soon as a stable nuclei is formed, i.e. particles larger than the critical size, they begin to grow into crystals of larger size. As atoms are added to the crystal for continuous growth, the solid/liquid interface takes on a specific structure at the atomic scale. [14] For silicon in aluminium alloys this structure is faceted growth. [19] Crystals having planar, angular surfaces (facets) is often formed by substances exhibiting complex crystal structures and directional bonding. [14]

For eutectic alloys containing a faceting minor phase, the morphology of the crystals during solidification may be sensitive to cooling/growth rate. [19] It is found that the average grain size of silicon crystals decreases as the solidification velocity increases. [20] At higher solidification velocities the refining will be affected, as the effective segregation coefficients of impurity will tend to unity, i.e. concentration of impurity in the solid silicon will approach that of the liquid melt. [21]

The morphology of the silicon crystals can be affected by the silicon composition in the Al-Si melt. This is because the silicon has a strong tendency to grow in the (111) plane combined with different nucleation conditions. It is the twin plane re-entrance edge (TPRE) mechanism that makes the silicon grow in the (111)

plane. In an alloy with low silicon content of 17wt%Si, star-shaped silicon crystals connected to a fish-bone structure are often observed, as viewed in Figure 2.5a. For higher silicon content around 22-25wt%Si, star-shaped crystals are observed as shown in Figure 2.5b. The star and fish-bone structures nucleate in a similar way, but the growth occurs differently depending on the composition. High silicon content of 38wt%Si in the alloy will result in crystals with plate-like structure growing in layers shown in Figure 2.5c and will be both longer and thicker at high silicon content. The layered growth of the silicon plates forms aluminium inclusions in the silicon crystals. [9] By controlling the crystal growth conditions, the Al inclusions in silicon crystals could be avoided. [7, 9]

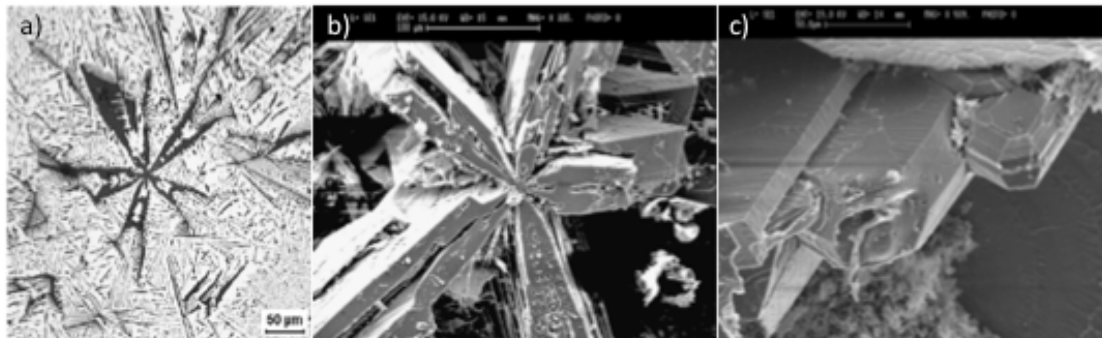

Figure 2.5, Silicon crystal morphologies: a) Light microscope image of star-shaped faceted crystal connected to fish-bone structure in a 17wt% Si sample, b) SEM picture of star-shaped silicon crystal with five arms growing from a common nucleus in a 25wt% Si sample, c) large plates of Si growing over each other in a 38wt% Si sample. [9]

The growth rate of silicon crystals in Al-Si melts can be found by directional solidification with different temperature gradients and cooling rates. If the growth rate, V, is assumed to be diffusion controlled it can be expressed by Equation 2.9 based on the steady-state diffusion equation of Si. [7]

$$V = D_{Si\ in\ Si-Al\ melt} \cdot \frac{\partial X_{Si\ in\ Si-Al\ melt}}{\partial x} \tag{2.9}$$

Where $D_{Si\ in\ Si\text{-}Al\ melt}$ is the diffusion coefficient of Si, $X_{Si\ in\ Si\text{-}Al\ melt}$ is the silicon content at the growth interface and x is the distance in the crystal growth

direction. When the temperature gradient is $\partial T/\partial x$ (K/m), Equation 2.9 can be rewritten as Equation 2.10. [7]

$$V = D_{Si\ in\ Si-Al\ melt} \cdot \frac{\partial X_{Si\ in\ Si-Al\ melt}}{\partial T} \cdot \frac{\partial T}{\partial x} \tag{2.10}$$

The term $\partial X_{Si\ in\ Si-Al\ melt}/\partial T$ are the slope of the liquidus curve that is without solidification of Si in the melt, which is shown by Figure 2.6. [22]

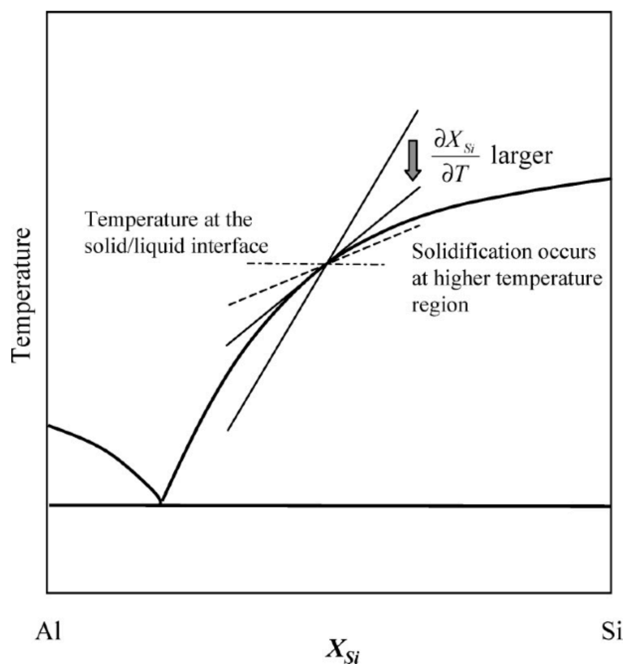

Figure 2.6, Estimation of $\partial X_{Si}/\partial T$ from the Al-Si phase diagram. [22]

In a flat crystal-melt interface the crystal growth is controlled by diffusion. The diffusion of silicon in the melt must be accelerated to achieve high-efficiency crystal growth. [7]

It is shown that the Al content in the Si crystals decreases with decreasing crystal growth rate as shown by Figure 2.2. At a low growth rate, the aluminium content corresponds to the maximum solid solubility of Al in solid Si, while higher growth rates gives a higher Al content. This indicates a possible entrapment of the Al-Si melt in the silicon crystals, [7] which occurs in crystals with plate-like growth as mentioned. [9]

It is also found that adjusting the initial weight of the alloy and the inner diameter of the crucible can control the growth rate, as the growth rate increases with an increase in the volume and a decrease in the cross-sectional area. [7]

2.2.3 Growth by directional solidification

Directional solidification takes place when the removal of both the heat necessary for the melt to cool down to the solidification temperature and the latent heat generated at the solidification interface due to the freezing, occurs along a single direction. [23]

Solidification of the alloy in the furnace depends on temperature gradients and pulling rates, which in turn determines the growth rates. By considering the movement of a planar solid/liquid interface along a bar of alloy, the distribution of impurities can be simplified. [17] If solidification is occurring at temperature T^*, the equilibrium at the interface requires that the liquid and solid composition during solidification, respectively C_L^* and C_S^*, are fixed by the phase diagram, see Figure 2.7a. At temperatures below the liquidus temperature, T_L, equilibrium can be attained at the solid-liquid interface, see Figure 2.7b. [16]

The distribution of the solute at the solid-liquid interface during solidification can be described by the equilibrium segregation coefficient, k, given in Equation 2.11. [16]

$$k = \frac{C_S^*}{C_L^*} \tag{2.11}$$

Where C_S^* is the content of solute in the solid phase and C_L^* is the content of solute in the liquid phase, both referring to the solid-liquid interface.

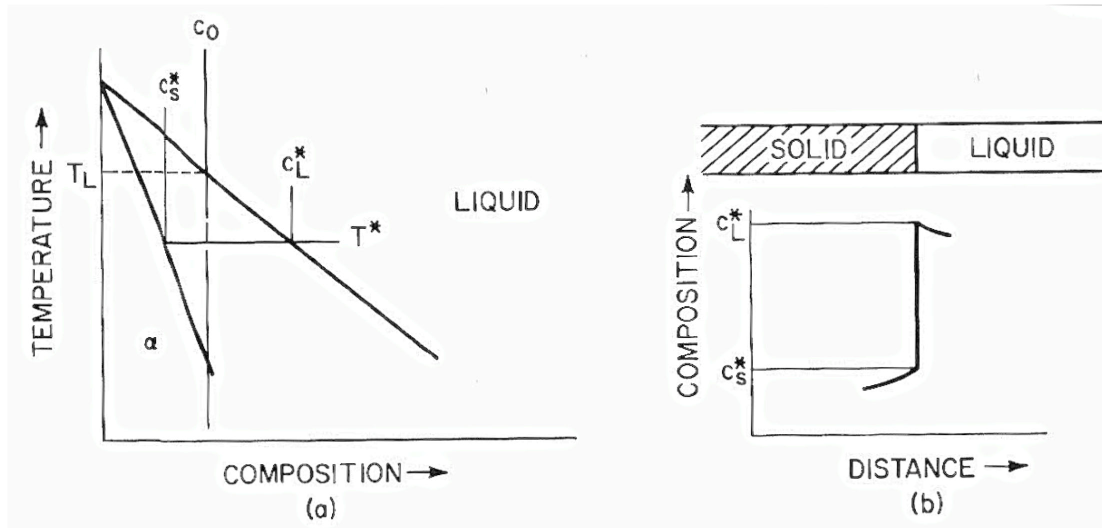

Figure 2.7, Solidification of an alloy with equilibrium at the solid-liquid interface. (a) Phase diagram where C_L^* and C_S^* are fixed at temperature T*. C_0 is the initial composition; (b) Composition profile of interface at equilibrium. [16]

The segregation coefficient for impurities present in silicon is in most cases lower than unity, meaning that the impurities will increase in the liquid phase as the solid rejects them. If the melt is relatively stagnant it will cause impurities to build up close to the solidification front, creating a boundary layer. [24] This boundary layer, with an assumed thickness δ, has a mass transport caused by diffusion only, and the liquid composition outside is maintained uniform by convection as viewed in Figure 2.8. [16]

Equilibrium refers to a growth speed of 0 mm/min or, more practically, very low growth rates. This combined with a boundary layer tend to give a reduced effective value of k, k_{eff} given in Equation 2.12. [16, 24]

$$k_{eff} = \frac{k}{k + (1-k)\exp - \left(\frac{v\delta}{D_L}\right)} \tag{2.12}$$

Where v is the growth rate and D_L is the element diffusivity in silicon. It can be seen that when $v \rightarrow 0$ or $D_L \rightarrow \infty$, $k_{eff} \rightarrow k$.

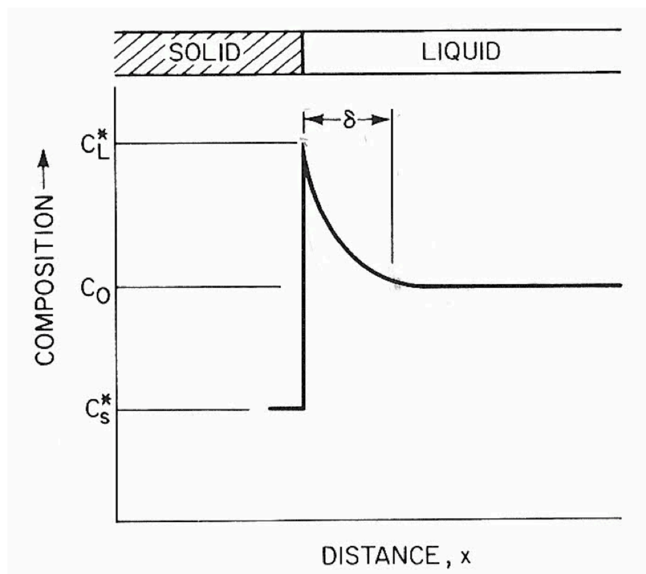

Figure 2.8, Solute profile showing the diffusion layer, δ, created in front of the interface by rejection of solute from solid to liquid phase. [16]

2.2.4 The solid-liquid interface

As mentioned, the solute will pile up ahead of the interface as the silicon crystal rejects it, when the segregation coefficient is less than unity. [14] Figure 2.9b shows this solute enriched layer in front of the solid-liquid interface. The interface is given by x´= 0. With increasing distance from the interface the solute content becomes lower and therefore the equilibrium liquidus temperature increases, as shown by Figure 2.9c. The curve must pass trough T* since equilibrium is assumed at the solid-liquid interface. This represents the condition necessary for stable plane front solidification.

Figure 2.9d depicts an unstable case where the liquid in the front of the interface has a temperature below the equilibrium liquidus temperature. This is called constitutional undercooling as it arises from a change in composition and results in instability of the plane front. [16]

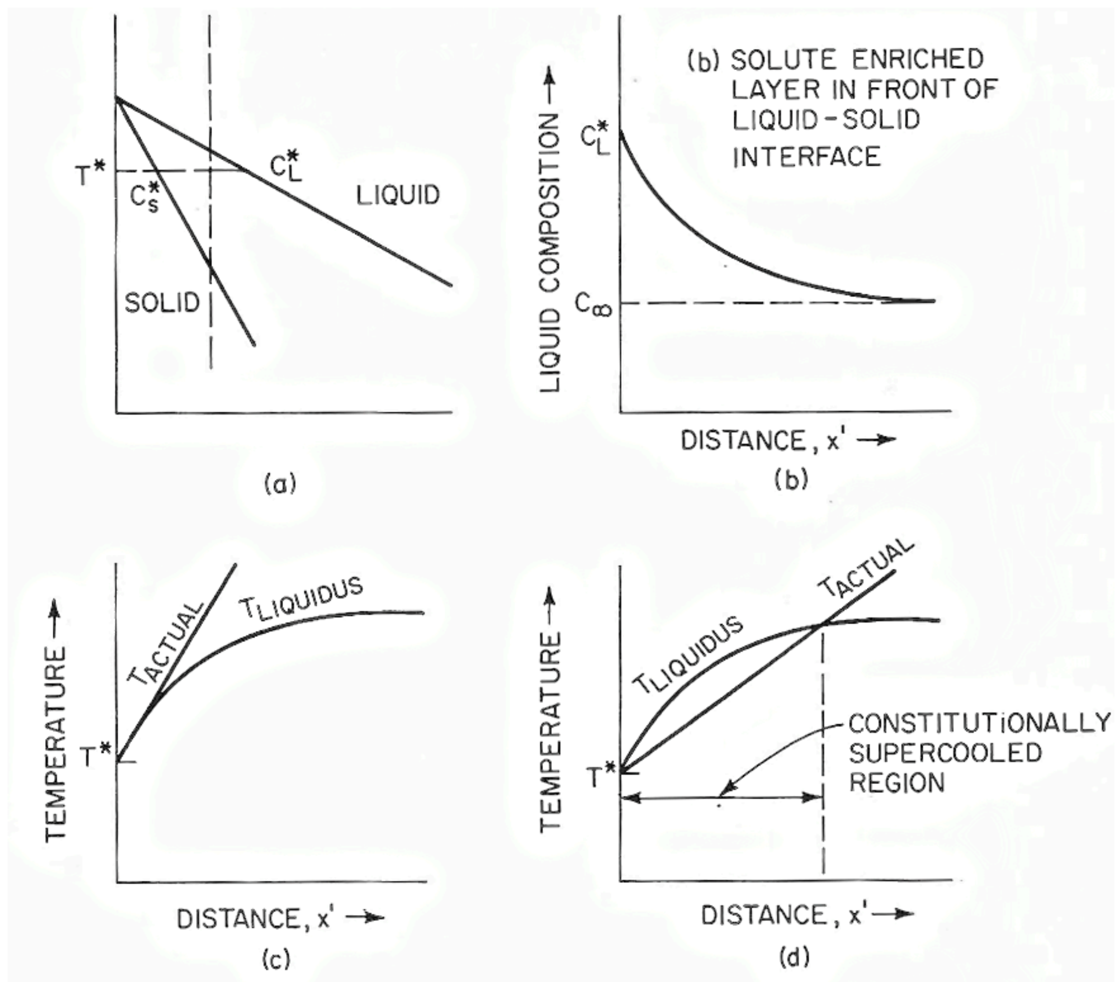

Figure 2.9, Constitutional undercooling in alloy solidification. (a) Phase diagram showing compositions at temperature T*, (b) solute enriched layer in front of liquid-solid interface, (c) stable interface where T_L increases with lower solute content while T_A is dictated by heat flow, (d) unstable interface where liquid immediately in front of the interface is at an actual temperature below T_L, termed constitutional undercooling. [16]

The condition required for a constitutionally undercooled zone is that the temperature gradient, G, at the interface in the liquid should be lower than the gradient of liquidus temperature change in the melt. The latter gradient is obtained by multiplying the concentration gradient, G_C, by the liquidus slope, m. If Equation 2.13 is valid, the interface is constitutionally undercooled and will therefor always become unstable. [14]

$$G < mG_C \tag{2.13}$$

A computer simulation showing the breakdown of a solid-liquid interface during directional solidification for a binary alloy is viewed in Figure 2.10. A plane solidification front is viewed in Figure 2.10a. Above the solidification front there will be a build up of impurities as mentioned and the solid profile will change gradually from planar to cellular as viewed in Figure 2.10b-e. A cellular solidification front as viewed in Figure 2.10f will be obtained which will influence the impurity distribution and grain size. This in turn will have an influence on the material quality, i.e. refining process. [24]

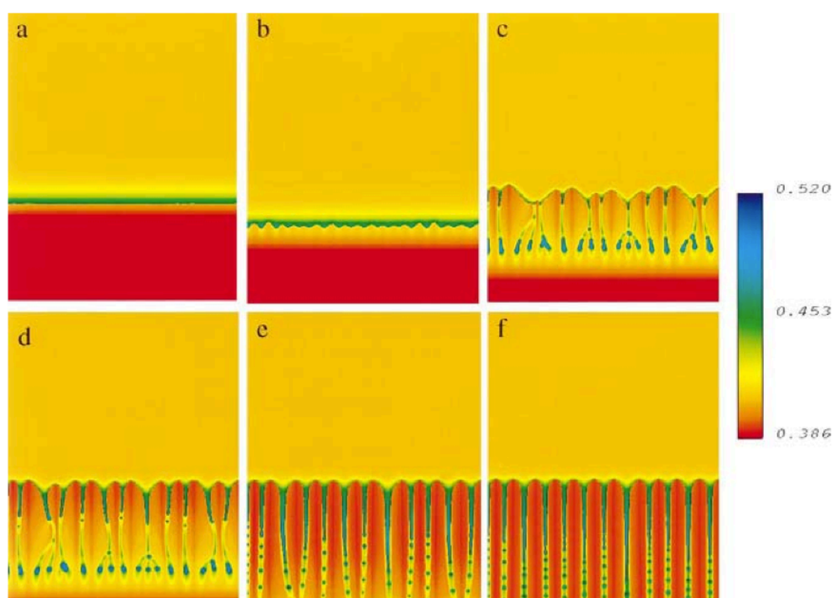

Figure 2.10, Computer simulation of the interface breakdown from planar into cellular. The concentration profile of the solute is shown in atomic fraction. The solidification growth velocity is 0,5cm/s. [24]

The limit of constitutional undercooling can be expressed by Equation 2.14. [14]

$$\frac{G}{V} = \frac{\Delta T_0}{D} \tag{2.14}$$

Where V is the rate of the interface movement, D is the diffusion coefficient in liquid and ΔT_0 is the liquidus-solidus range at C_0. G and V are the main variables that determine the form and scale of the various microstructures obtained by

using a typical alloy. These are shown in Figure 2.11. In directional growth, the cooling rate $|\dot{T}|$ is given by Equation 2.15. [14]

$$|\dot{T}| = G \cdot V \qquad (2.15)$$

From Figure 2.11 the temperature gradient, G, or growth rate, V, are varied to present different solidification morphologies. The ratio, G/V, represents a constancy of microstructure and largely determines the growth morphology. G·V on the other hand indicate a constant scale for these structures. [14]

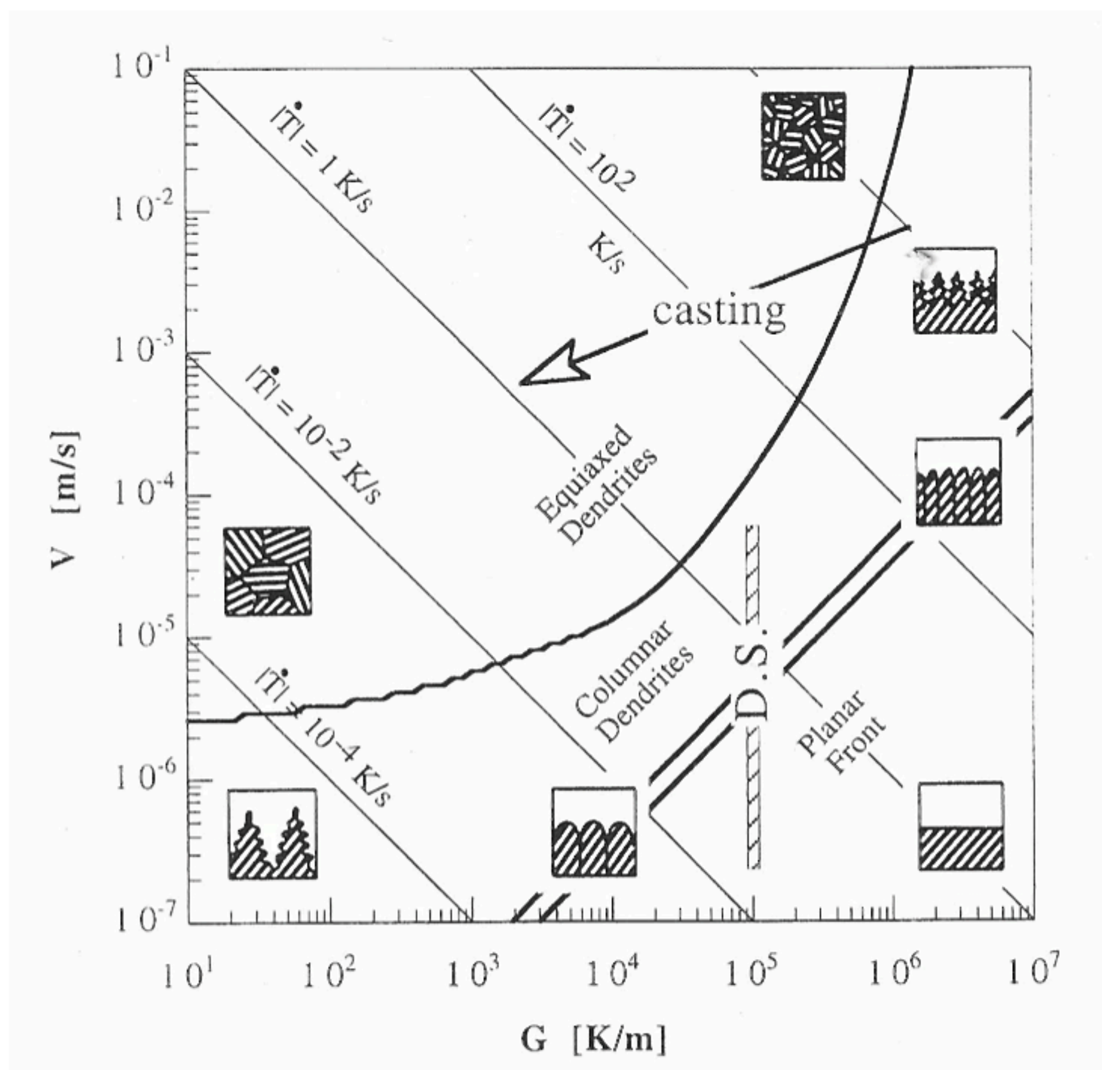

Figure 2.11, Schematic diagram of different solidification morphologies depending on cooling rate, $|\dot{T}|$. The vertical directional solidification line, D.S., can be used to tailor conditions for optimizing material properties. [14]

2.2.5 Seeded growth of silicon crystals

The use of seed from mono-crystalline silicon, with a given orientation for the growth of silicon crystals, will be discussed here. No papers are to be found regarding seeded growth of silicon crystals from an Al-Si melt, however the use of seed to grow silicon crystals in silicon melt is a commonly used method.

The Czochralski process is the most widely used method for crystal growth of electronic and optical materials. A single crystal seed with the desired orientation is dipped into the silicon melt and a reduction in temperature allows the growth of a single crystal with same orientation as the seed, as it is pulled upwards from the melt. [25]

The Bridgeman process can be used to grow both mono-crystalline and multi-crystalline silicon. To grow mono-crystalline Si, a seed is placed in the bottom of the crucible and lowered downwards in the furnace to initiate crystal growth from the seed. [25] For multi-crystalline growth there is no seed, but the crucible is slowly lowered downwards in the furnace out of the inductively heated hot zone. This is called conventional Bridgman technique and is the most widely used process for fabrication of multi-crystalline ingots. [26]

For both Czochralski and Bridgeman process a seed with a given orientation is used to control the growth of silicon crystals. Figure 2.12 show a setup where the silicon seed crystal is composed of two different orientations, <100> and <111>. Crystal growth starts at both seed crystals and grow with the orientation given by the seed. Such experiments, where the seed is designed to cause a grain boundary, are used to observe multi-crystalline silicon growth so that the growth process can be optimized. [27]

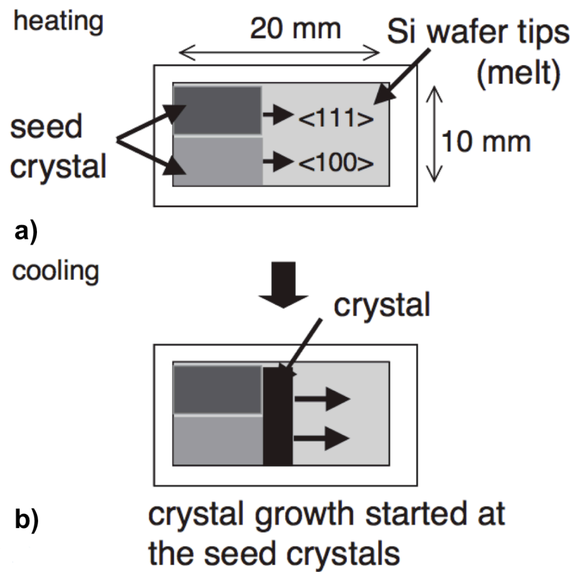

Figure 2.12, Schematic illustration of seeded growth. a) Seed consisting of two different orientations b) Crystal growing with two different orientations given by the seed. Modified from [27]

2.3 Refining of silicon in Al-Si melt

For solar grade silicon (SoG-Si) a purity of 6-7N is required, since the solar cell efficiency decrease as impurities shorten the lifetime of excited carriers in the solar cell and disturb the electric generation. [28] To reduce the impurity concentration in metallurgical grade silicon (MG-Si), a solvent refining method can be applied, where the solvent is aluminium as previously discussed.

2.3.1 Segregation ratio of impurities

When aluminium is alloyed with silicon it lowers the melting point as can be seen from the liquidus curve above the eutectic point, viewed in Figure 2.13.

Most impurities have retrograde solubilities in silicon, which means that the solid solubility will decrease with decreasing temperature above the eutectic. As the solvent refining technique with Al-Si melt can be performed at lower temperatures, this can be utilized. The retrograde solubility indicates thermodynamic instability of impurities at lower temperatures, [7] which can be seen from Figure 2.14.

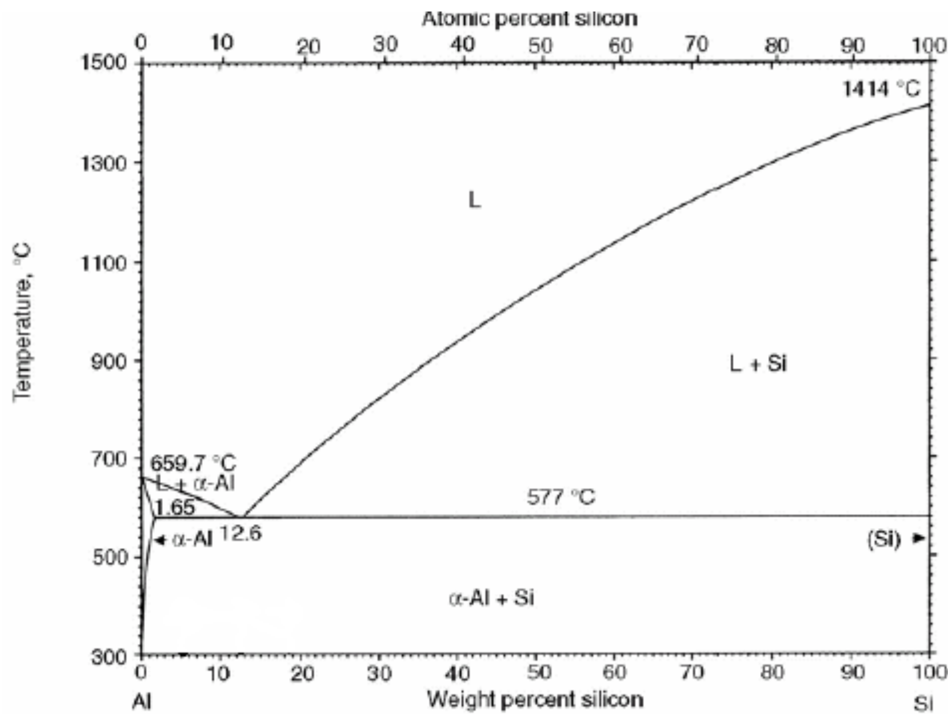

Figure 2.13, The Al-Si equilibrium phase diagram. The eutectic point in this binary system is found at 12,6wt%Si. Modified from [29]

During cooling of hypereutectic Al-Si melts, the silicon crystals grow, and impurity elements are subject to solid/liquid segregation. The Al-Si system has a low eutectic temperature, and gives effective removal of impurities as the segregation tendency is enhanced at low temperatures as discussed above. Segregation ratios of impurities between solid silicon and Al-Si solvent are essential in order to know the refinability during the solidification process. The segregation ratio, k_i, given in Equation 2.16 is defined as the molar ratio of impurity i in solid silicon to solvent. [30]

$$k_i = \frac{x_{i\ in\ solid\ silicon}}{x_{i\ in\ solvent}} \qquad (2.16)$$

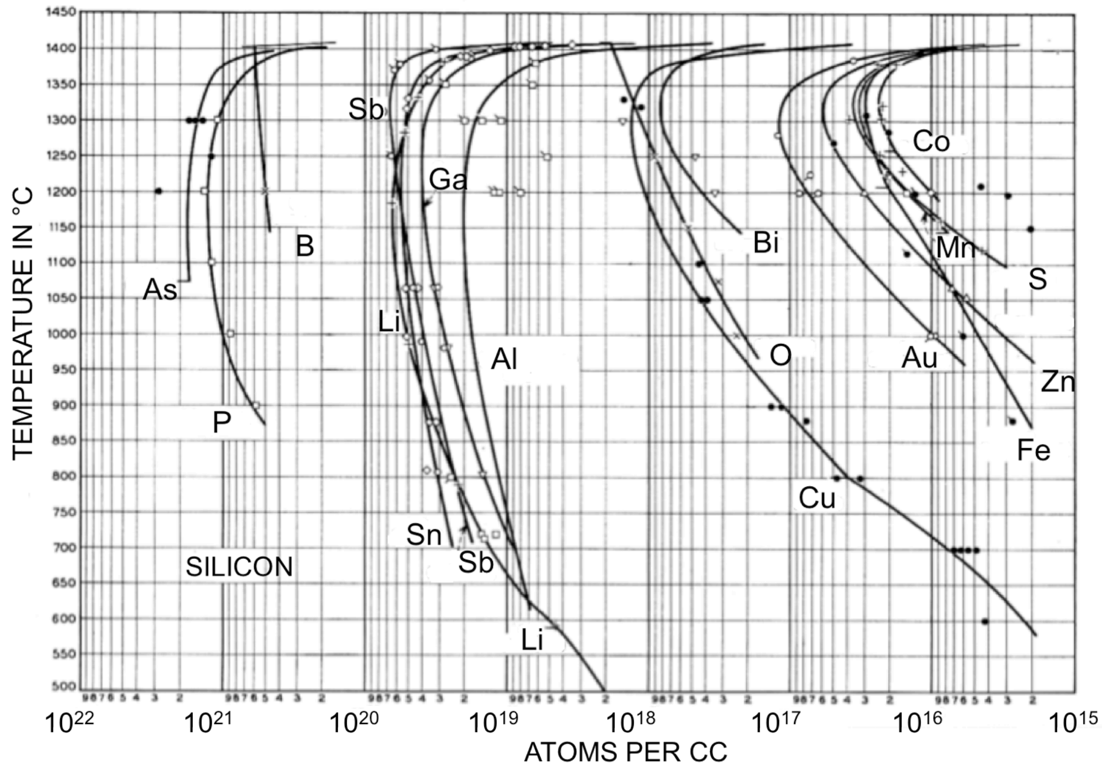

Figure 2.14, Solid solubility of different impurities in silicon. The solid solubility decreases with decreasing temperature. Modified from [31]

The thermodynamic approach expressed in Equation 2.17 and 2.18 can be used to calculate the segregation ratios of metallic impurities between solid silicon and Al-Si solvent. [30]

$$\mu_i\,(l) = \mu_i\,(s) \tag{2.17}$$

$$\mu_i^0\,(l) + RT\ln a_{i\;in\;Al-Si\;solvent}\,(l) = \mu_i^0\,(s) + RT\ln a_{i\;in\;solid\;silicon}\,(s) \tag{2.18}$$

where μ_i^0 and a_i are the chemical potential at the standard state and the activity of the impurity element i, respectively. Rearrangement of Equation 2.18 gives Equation 2.19, expressing the segregation ratio. [30]

$$\ln k_i = \ln\frac{x_{i\;in\;solid\;Si}}{x_{i\;in\;Al-Si\;solvent}} = \frac{\Delta G_i^{fus}}{RT} + \left(\bar{G}^{ex}_{i\;in\;Al-Si\;solvent}\,(l) - \bar{G}^{ex}_{i\;in\;solid\;silicon}\,(s)\right) \tag{2.19}$$

where ΔG_i^{fus} denotes the Gibbs free energy change for fusion of the impurity element. The excess Gibbs free energy of the impurity element in Al-Si solvent, $\bar{G}_{i\ in\ Al-Si\ solvent\ (l)}^{ex}$ is estimated from the Gibbs free energies of the binary Al-Si, Al-i and Si-i melts while the excess Gibbs free energy of the impurity element in solid silicon, $\bar{G}_{i\ in\ solid\ Si\ (s)}^{ex}$ is determined from its solid solubility. [30]

Table 2.1, Calculated segregation ratios of metallic impurity elements between solid silicon and the Si-Al melt at 1073-1473 K with segregation coefficients between solid and liquid silicon. [32]

Element	Segregation ratio between solid silicon and Si-Al melt			Segregation coefficient between solid and liquid silicon at its melting point
	1073 K	1273 K	1473 K	
Iron	$1{,}7 \cdot 10^{-11}$	$5{,}9 \cdot 10^{-9}$	$3{,}0 \cdot 10^{-7}$	$6{,}4 \cdot 10^{-6}$
Titanium	$3{,}8 \cdot 10^{-9}$	$1{,}6 \cdot 10^{-7}$	$9{,}6 \cdot 10^{-7}$	$2{,}0 \cdot 10^{-6}$
Chromium	$4{,}9 \cdot 10^{-10}$	$2{,}5 \cdot 10^{-8}$	$2{,}5 \cdot 10^{-7}$	$1{,}1 \cdot 10^{-5}$
Manganese	$3{,}4 \cdot 10^{-10}$	$4{,}5 \cdot 10^{-8}$	$9{,}9 \cdot 10^{-7}$	$1{,}3 \cdot 10^{-5}$
Nickel	$1{,}3 \cdot 10^{-9}$	$1{,}6 \cdot 10^{-7}$	$4{,}5 \cdot 10^{-6}$	$1{,}3 \cdot 10^{-4}$
Copper	$9{,}2 \cdot 10^{-8}$	$4{,}4 \cdot 10^{-6}$	$2{,}5 \cdot 10^{-5}$	$4{,}0 \cdot 10^{-4}$
Zinc	$2{,}2 \cdot 10^{-9}$	$1{,}2 \cdot 10^{-7}$	$2{,}1 \cdot 10^{-6}$	$1{,}0 \cdot 10^{-5}$
Gallium	$2{,}1 \cdot 10^{-4}$	$8{,}9 \cdot 10^{-4}$	$2{,}4 \cdot 10^{-3}$	$8{,}0 \cdot 10^{-3}$
Indium	$1{,}1 \cdot 10^{-5}$	$4{,}9 \cdot 10^{-5}$	$1{,}5 \cdot 10^{-4}$	$4{,}0 \cdot 10^{-4}$
Antimony	$3{,}4 \cdot 10^{-3}$	$3{,}7 \cdot 10^{-3}$	$8{,}2 \cdot 10^{-3}$	$2{,}3 \cdot 10^{-2}$
Lead	$9{,}7 \cdot 10^{-5}$	$2{,}9 \cdot 10^{-4}$	$1{,}0 \cdot 10^{-3}$	$2{,}0 \cdot 10^{-3}$
Bismuth	$1{,}3 \cdot 10^{-6}$	$2{,}1 \cdot 10^{-5}$	$1{,}7 \cdot 10^{-4}$	$7{,}0 \cdot 10^{-4}$

Segregation ratios of impurities between solid silicon and the Al-Si melt give the purification during solidification. These are calculated by Equation 2.19 for different metallic impurities at different temperatures (1073 K - 1473 K) and shown in Table 2.1. [32] To compare, the segregation coefficients between solid and liquid silicon at its melting point is also tabulated. The segregation coefficients are larger than the segregation ratios, and the segregation ratios decrease with decreasing temperature, which means that the solidification refining with Al-Si melt has a higher effect at low temperatures. The segregation ratios are far less than unity, which means that they are more soluble in the liquid phase than in the solid phase. Most of the metallic impurities segregate out

at silicon grain boundaries and acid leaching is an effective method to remove these impurities. [8]

Boron and phosphorus are difficult impurities to remove with ordinary solidification refining because of their high segregation coefficients in silicon, 0,80 for boron and 0,35 for phosphorus. [32] Yoshikawa and Morita [32] have shown that alloying silicon with aluminium also causes a decrease in the segregation ratios for these elements, viewed in Figure 2.15. The segregation coefficients are also shown in the figure. The segregation ratio of boron at its infinite dilution between solid silicon and Si-Al melt was determined to 0,49 at 1473 K, 0,32 at 1373 K and 0,22 at 1273 K. [33] For phosphorus the segregation ratios was determined to 0,12 at 1373 K, 0,085 at 1273 K and 0,061 at 1173 K at its infinite dilution. [34] This shows that the segregation ratios for boron and phosphorus will decrease with decreasing temperature as for the metallic impurities. [32]

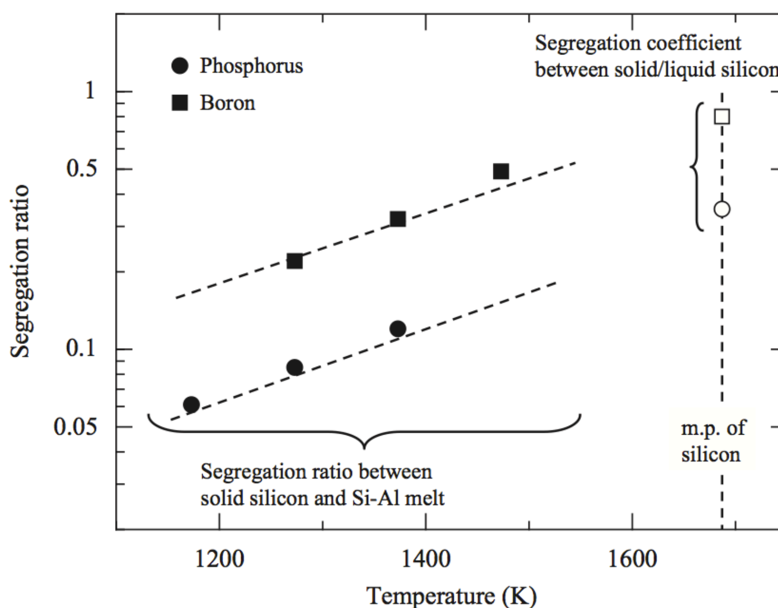

Figure 2.15, Temperature dependence of segregation ratios of phosphorus and boron between solid silicon and Si-Al melt. Segregation coefficient between solid/liquid silicon is also shown. [32]

2.3.2 Refining by directional solidification

Directional solidification can be used as a refining step of the liquid to be solidified, and can be applied to solidification of Al-Si melt.

The distribution of impurities in the solidifying silicon when directional solidification is applied can be illustrated by the Gulliver-Scheil´s equation, first some assumptions must be considered, [16, 35]

1. The convection and diffusion in the melt are so violent and rapid that the melt at every moment has an even composition, i.e. complete equilibrium in the liquid phase;
2. The diffusion in the solid phase is so slow that it can be completely neglected;
3. Local equilibrium exists between the solid phase and the melt.

At temperature T^*,solid of composition C_S^* is freezing from liquid of composition C_L^* and the solute content will be higher in the liquid. In later stages of the solidification, the solid that forms will have a higher solute content as diffusion in the solid is neglected. The solute distribution along the length of the growing crystal is as shown in Figure 2.16. [16]

When a small amount of solid forms, the solute is rejected by the solid-liquid interface and results in a solute increase in the liquid. By ignoring the difference in molar volume between the solid and liquid this balance is given in Equation 2.16. [16, 17]

$$(C_L - C_S^*)df_s = (1 - f_s)dC_L \qquad (2.16)$$

Where f_S is the volume fraction solidified.

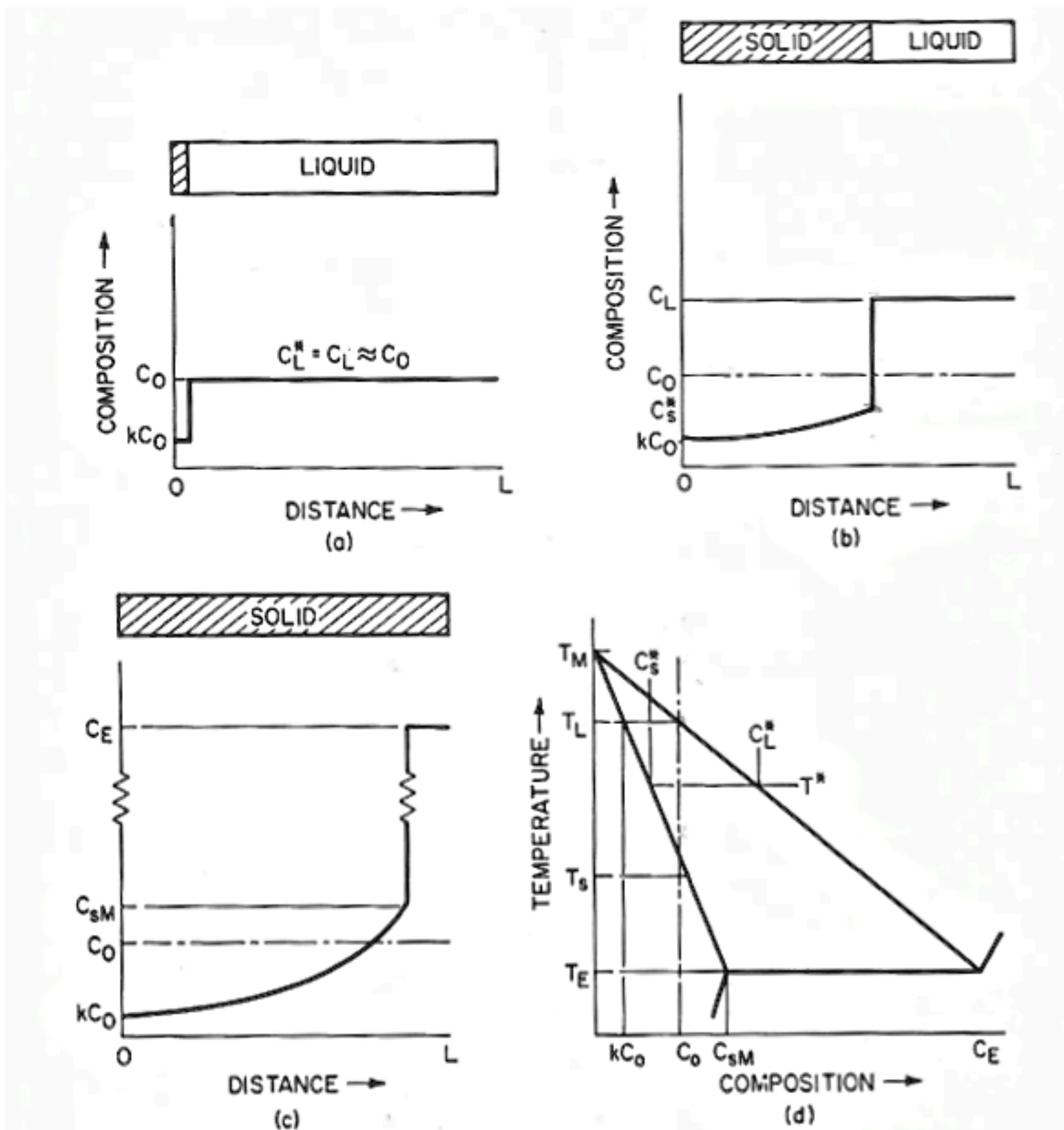

Figure 2.16, Composition profile of solute along a bar of length L solidifying directionally from left to right, under assumption of complete mixing in the liquid and no diffusion in the solid phase when interface is at equilibrium. (a) profile at the beginning of the solidification, (b) profile at temperature T* where no diffusion in the solid gives the composition kC_0 at the very first solid formed, (c) profile at end of solidification where the last part to be solidified has an eutectic composition, (d) phase diagram. [16]

C_0 is the initial concentration, so integrating this equation using the boundary condition $C_S^* = kC_0$ when $f_s = 0$ gives the composition of the solid at the solid-liquid interface as a function of fraction solid, as shown in Equation 2.17. [16, 17]

$$C_S^* = kC_0(1 - f_S)^{(K_0 - 1)} \quad (2.17)$$

Equation 2.17 is known as the Gulliver-Scheil´s equation and is a useful tool regarding preliminary evaluation of the refining possibilities of silicon during directional solidification. Even though a planar solid-liquid interface is considered, this equation is applicable for non-planar solid-liquid interfaces provided that the liquid composition is uniform and that the Gibbs-Thompson effect is negligible. [17]

If the effective value of k, k_{eff}, is taken into account Equation 2.17 can be rewritten as follows. [16]

$$C_S^* = k_{eff} C_0 (1 - f_s)^{(k_{eff} - 1)} \tag{2.18}$$

At high growth rates and/or no melt convection, the effective segregation coefficient moves towards unity and no solute segregation occurs. [36]

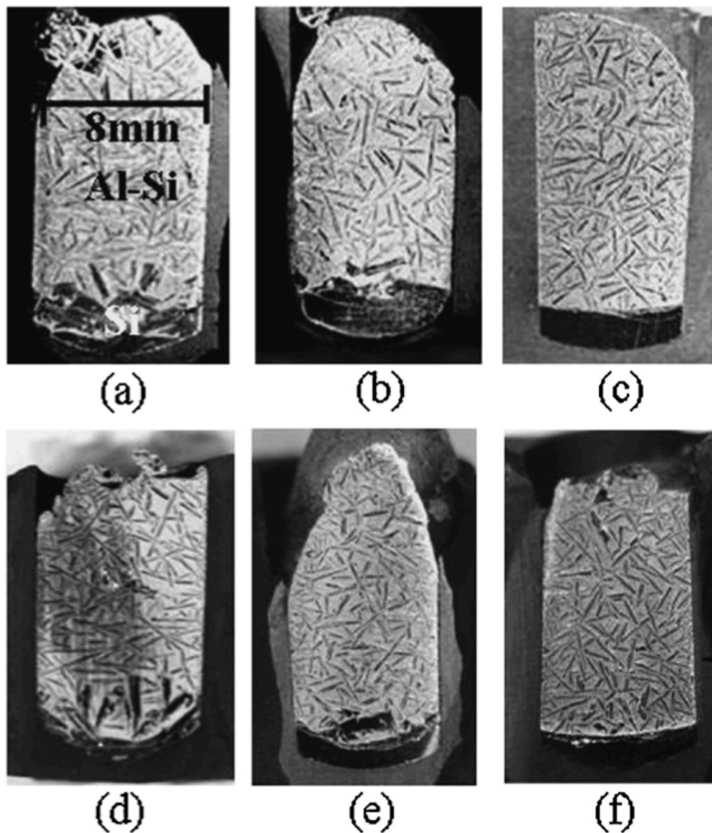

Figure 2.17, Photographs of cross sections of samples solidified directionally. Temperature gradient: 1,5 K/mm. Cooling rate (a) 0,105, (b) 0,084, (c) 0,031 K/min. Temperature gradient: 4,0 K/mm. Cooling rate (d) 0,273, (e) 0,194, (f) 0,08 K/min. [7]

Directional solidification was carried out by Nishi, Kang and Morita [7] to obtain bulk silicon crystals from Al-Si melt. They used a resistance furnace with a PID-control system in argon atmosphere, where argon was purified and dried by passing it over silica gel, magnesium perchlorate and soda lime. Material with an alloy composition of Si-55,3at%Al were melted in a graphite crucible at 1323 K. The sample was cooled to 1173 K in a temperature gradient of 1,5-4,0 K/mm and cooling rates as given in Figure 2.17. The crystal-melt interface was classified as rough in sample (a) and (d), intermediate in sample (b) and (e) and flat in sample (c) and (f). The purpose was to obtain bulk Si crystals from the Al-Si melt and this was managed in samples with flat interface as no melt remnant was found in the crystals.

Silicon crystals were found to grow near the bottom of the sample and it was found that as the cooling rate decreases the crystal-melt interface became more planar. The refining efficiency of boron and phosphorus was found to be more or less 90% whereas 99% of iron and titanium was removed. [7] Yoshikawa and Morita [33] also found the removal fraction of boron to be 90% by the use of temperature-gradient-zone-melting. However, they concluded that further treatment for boron removal is necessary to achieve a low-cost silicon refining process.

2.4 Acid leaching

The purification of silicon crystals is as much a function of the aluminium removal as the segregation coefficient, since the impurities are gathered in the aluminium. [37] Acid leaching is a method to remove inter-grains contaminants so that silicon crystals can be collected, but it is difficult to remove all the material surrounding the crystals. [7, 37]

Liu and co-workers [38] has focused their work with Al-Si alloying on the removal of boron combined with acid leaching to improve the refining efficiency. They melted together MG-Si powder and 99% Al powder to Al-21wt%Si alloy. The material was heated to 727°C and held for 6 hours before the temperature

was lowered to 600°C and held for 2 hours. They found that the gravity force method was effective for refining of silicon by Al-Si alloying. The removal rate of boron was determined to 78,42% by solvent refining with aluminium, whereas the removal rate increased to 89,21% after acid leaching with diluted hydrofluoric acid.

2.5 Electromagnetic separation

Electromagnetic separation can be used to separate silicon crystals from the Al-Si melt. By agglomerating the silicon crystals to one part of the melt, the following acid leaching can be simplified. [22]

Solid silicon has a relatively low electrical conductivity ($\sigma_S = 5 \cdot 10^4\ S/m$), [39] while aluminium melt has a higher electrical conductivity ($\sigma_L = 2{,}95 \cdot 10^6\ S/m$). [40] Such high difference in electrical conductivity makes it possible to separate the silicon crystals from the melt by imposing an electromagnetic field. This is because the applied uniform electromagnetic force compresses the liquid metal and a pressure gradient is generated. The low electrical conductivity of the silicon crystals experiences a lower electromagnetic force meaning that they mostly receive the pressure force. This is simply shown in Figure 2.18. [39]

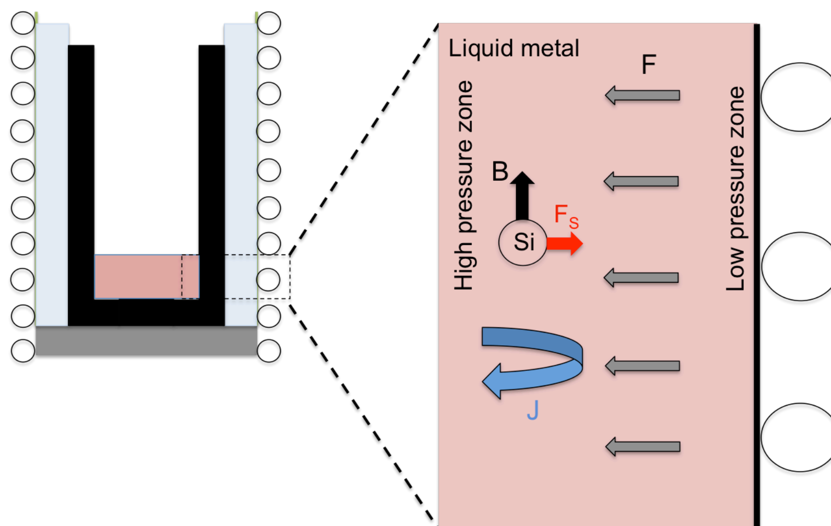

Figure 2.18, Graphical presentation of the principle behind the electromagnetic separation of silicon crystals from the liquid metal by the inserted electromagnetic forces. Modified from [39]

Equation 2.19 can describe the force acting on the silicon crystals in the melt, which for simplicity is assumed to be a sphere. Note that the equation requires different electrical conductivity on the sphere and the liquid. [39]

$$\vec{F}_S = -\frac{3}{2} \cdot \frac{\sigma_L - \sigma_S}{2\sigma_L + \sigma_S} V_S \vec{F} \tag{2.19}$$

Where F_S is the separation force acting on a sphere, V_S is the volume of the sphere and F is the electromagnetic force given by,

$$\vec{F} = \left|\vec{J} \times \vec{B}\right| \tag{2.20}$$

J is the induced current density and B is the magnetic flux density. Interaction between the induced current in the melt and the magnetic field created due to current that pass through the induction coil, leads to the generation of electromagnetic forces in the melt. [39] It is the alternating current, which is fed through the induction coil, that generates an alternating magnetic field which runs parallel to the center line of the coil. An alternating current in the load induced by this magnetic field runs in closed loops perpendicular to the center line of the coil and in such direction as to oppose the original magnetic field. This magnetic field cause stirring of the melt as shown in Figure 2.19. The current induced near the surface will largely neutralise the field in the interior of the load, hence the greater part of the current will be near the surface. This is known as the skin effect. [41]

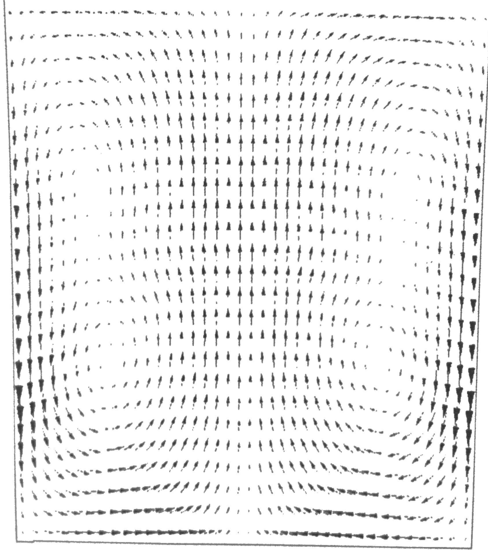

Figure 2.19, Velocity flow pattern in the central vertical cross section of a crucible due to magnetic field. [39]

The skin depth, δ, where the induced electromagnetic force should be restricted is given by Equation 2.21. [39]

$$\delta = \frac{1}{\sqrt{\pi f \mu_L \sigma_L}} \tag{2.21}$$

Where μ_L is the relative permeability of the liquid and f is the frequency. As can be seen from the equation, the skin depth decreases with increasing frequency. The electromagnetic force ensures good mixing in the liquid and is effective to carry the particles from the bulk of the liquid to the vicinity of the wall, where strong electromagnetic forces capture them within the skin depth, as shown in Figure 2.19. [39]

It is likely that the crystals will float when holding in the furnace, because the density of the silicon crystals (2330 kg/m^3) is lower than the Al-Si melt (2430 kg/m^3). [9] The velocity of the crystals, assuming that the crystal is spherical, is given in Equation 2.22. [40]

$$u_c = \frac{d_c^2 \Delta\rho g}{18\mu} \tag{2.22}$$

Where u_c is the ultimate settling velocity, d_c is the diameter of the crystal, $\Delta\rho = \rho_s - \rho_l$ is the density difference between silicon crystal (ρ_s) and melt (ρ_l), g is the acceleration of gravity and μ is the kinetic viscosity of melt.

If an electromagnetic force is present, the terminal migration velocity of the crystal, $u_{cm,\infty}$ can be found by Equation 2.23. It is assumed that the electromagnetic force acts in the horizontal plane so that the effect of gravity can be eliminated. [40]

$$u_{pm,\infty} = -\frac{d_c^2 F}{24\mu} \tag{2.23}$$

ϕ is the ratio between the terminal migration velocity and the ultimate settling, given in Equation 2.24. This is to compare the electromagnetic separation and natural settling and it can be seen that the electromagnetic expulsive force takes the place of the apparent gravity force to separate silicon crystals from the melt. [40]

$$\phi = \left|\frac{u_{cm,\infty}}{u_c}\right| = \left|\frac{3}{4}F\right| / \Delta\rho g \tag{2.24}$$

Yoshikawa and Morita [22] investigated the separation of silicon crystals in Al-Si melt by induced electromagnetic field. They positioned the crucible 3 cm below the lower end of the induction coil in the induction furnace. This would cause the silicon crystals to agglomerate near the bottom of the crucible and not near the crucible walls as just mentioned. In addition the sample was directionally solidified downwards with the rate of 0,25-1,0 mm/min.

Figure 2.20a explains this agglomeration of silicon crystals. Here the electromagnetic force, F, is generated toward the center of the melt since the crucible is placed below the induction coil. There are two main mechanisms that

occur. The temperature gradient driven to the perpendicular direction from the difference in induced current intensity, which gives solidification of silicon near the bottom of the sample, and a downward fluid flow induced from the inward Pinch force, which agglomerates the silicon crystals. Such agglomeration of silicon crystals to the bottom of the sample is shown in Figure 2.20b. [22]

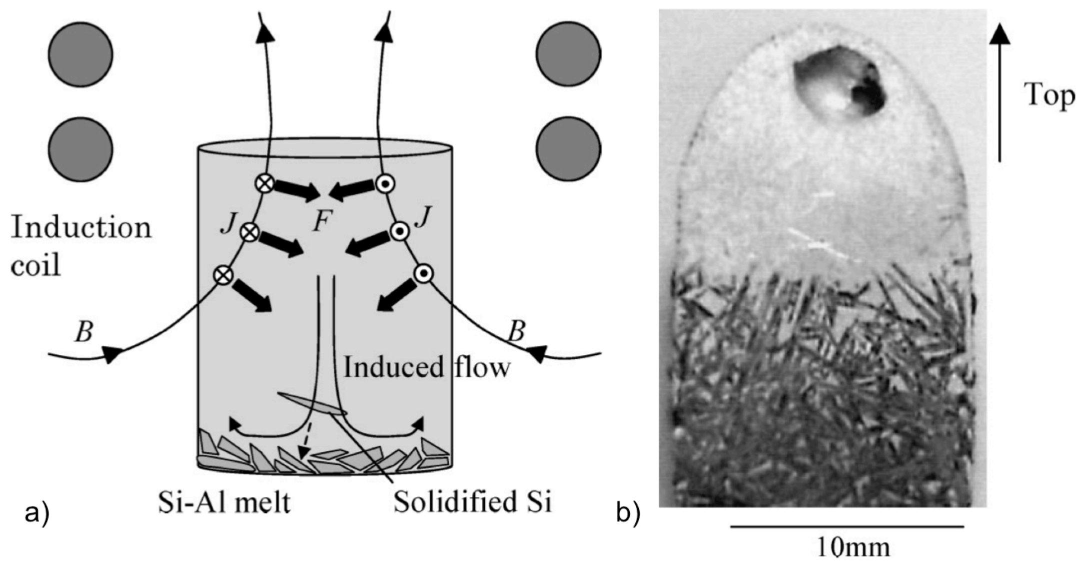

Figure 2.20, a) Mechanism for separation of Si grains solidified from Si-Al melt with electromagnetic field, b) Cross section photo of Si-55,3at%Al alloy solidified under the electromagnetic field. [22]

3 Experimental work

In this section, the different experiments carried out are presented and temperature measurements during the experiments are included. The experimental equipment that were used, which is the resistance furnace and induction furnace are presented. Overview of starting material together with analyses is given. Preparation of samples and analysing techniques such as light microscopy, EBSD in SEM and EPMA that are employed to the samples are presented.

3.1 Overview of experiments

There were performed eight experiments in total, which could be divided into four groups; DS, SG, SGS and IH. Table 3.1 gives an overview of experiments conducted with silicon content, pulling rate, weight of material and melting temperature. The DS experiments were conducted to find the largest growth of primary silicon crystals by varying silicon content and pulling rate. They are named DS experiments as the Al-Si alloy is solidified by directional solidification in a resistance furnace.

To investigate whether primary silicon crystal growth could be increased by addition of a mono-crystalline Si seed, the SG experiments were conducted. The Al-Si alloy was also here solidified by directional solidification in a resistance furnace. The difference from the DS experiments is the seeded growth and the stirring of the melt. In the three experiments there was performed no stirring, moderate stirring during experiment and melting with extensive stirring prior to the experiment. It was believed that the stirring would remove the oxide layer at the interface melt-seed, which is the reason for including it as a parameter.

The seeded growth was also performed with pure silicon, with the intention of investigating whether it was possible to grow silicon crystals from a seed without the aluminium present. This experiment is named SGS, seeded growth

with silicon. Also here the silicon is solidified directionally in a resistance furnace.

To investigate the separation of silicon crystals from the Al-Si melt by electromagnetic force, one experiment was performed in an induction furnace. The experiment is named IH because of the induction heating.

Table 3.1, Overview of performed experiments.

Experiment	Si content (wt%)	Pulling rate (mm/min)	Weight Al-Si (g)	Weight mono-Si (g)	Melting temperature (°C)
DS-1	18,5	0,18	47,87	–	1217
DS-2	35	0,18	43,39	–	1197
DS-3	35	0,12	44,17	–	1198
SG-1	35	0,18	43,33	16,25	910
SG-2	35	0,18	47,07	15,66	930
SG-3*	35	0,18	44,02	13,69	930
SGS-1	100	4,8	Si: 69,35	35,84	1420
IH-1	35	–	298,14	–	1227

* One part of the seed and the Al-Si alloy were melted together in a casting furnace before the directional solidification experiment.

3.2 Equipment

The equipment used in this thesis was a resistance furnace where most of the experiments were conducted and an induction furnace.

3.2.1 Resistance furnace

The first seven experiments listed in Table 3.1 were performed in a vertical resistance tube furnace with a pulling device for directional solidification, as shown in Figure 3.1. The furnace consists of a graphite heating element that works as a resistor with resistance, R, where a current, I, is passed through generating the thermal power, W, given by Equation 3.1. [41]

$$W = RI^2 \quad (3.1)$$

The power input is controlled by a S-type thermocouple that works in conjunction with a PID controller (Eurotherm, model 2416). This thermocouple is placed in the side of the vertical tube furnace, outside the heating element, shown by letter f in Figure 3.1. It is therefor measuring a temperature lower than the actual temperature inside the furnace and another thermocouple is necessary to monitor the temperature. This is done by a S-type thermocouple positioned at the bottom of the crucible, shown by letter i in Figure 3.1, which sends temperature information to a Micrologger (Campbell Scientific LTD). The sample rod is connected to a motorised puller, shown by letter m in Figure 3.1, lowering the crucible downwards for directional solidification.

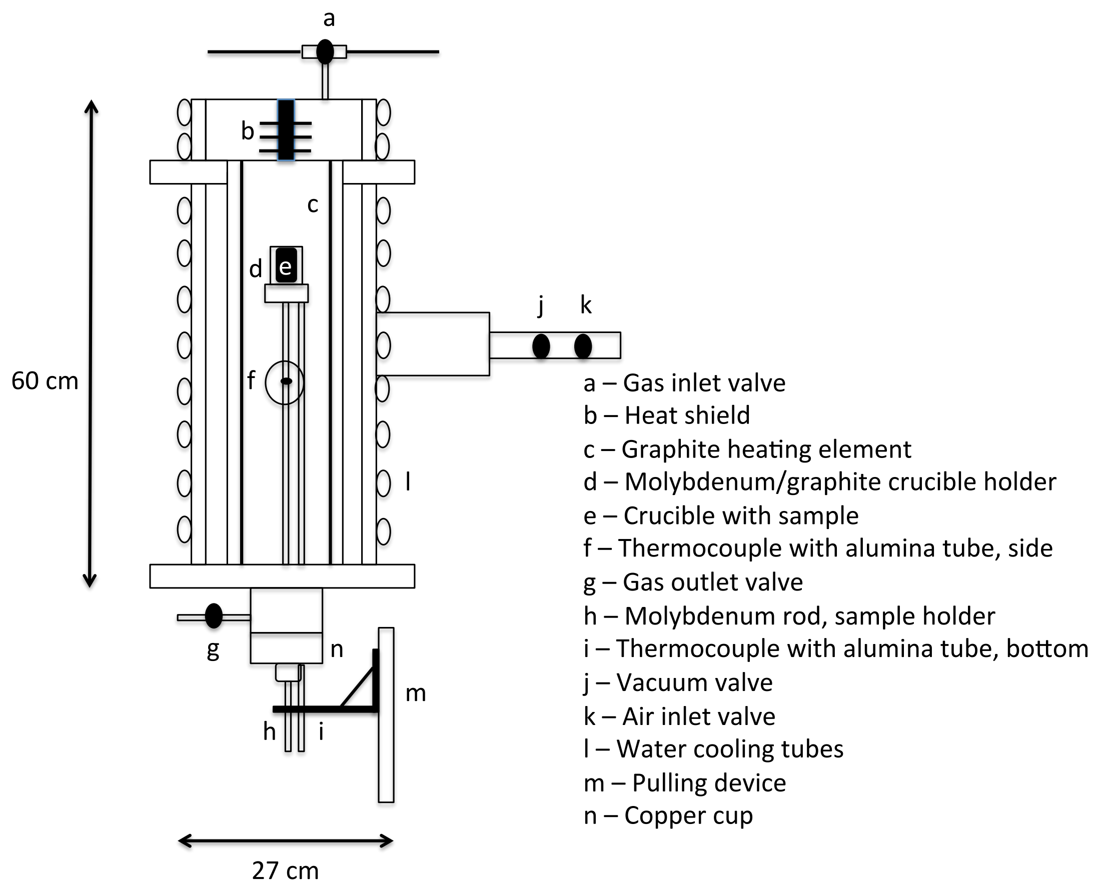

Figure 3.1, Sketch of resistance furnace, where a-n are the different components of the furnace.

The graphite heater requires a non-oxidizing atmosphere. [41] The furnace is equipped with a vacuum pump to evacuate the furnace chamber, which is then

backfilled by purging argon gas to reach an atmospheric pressure. The argon atmosphere is retained during the experiments. Flowing atmosphere in the furnace chamber during experiments has some advantages compared to static atmosphere, as the gas in the furnace is continuously replaced by clean argon gas. A flow meter is used for controlling the argon gas flow rate.

Two temperature profiles of the resistance furnace were obtained by a hold at each cm in the furnace until the temperature stabilized. The temperatures are given in distance above the copper cup and are shown in Figure 3.2. A furnace temperature of 1200°C was used for DS experiments, while a lower temperature of 1000°C was used for SG experiments to avoid complete melt down of the seed.

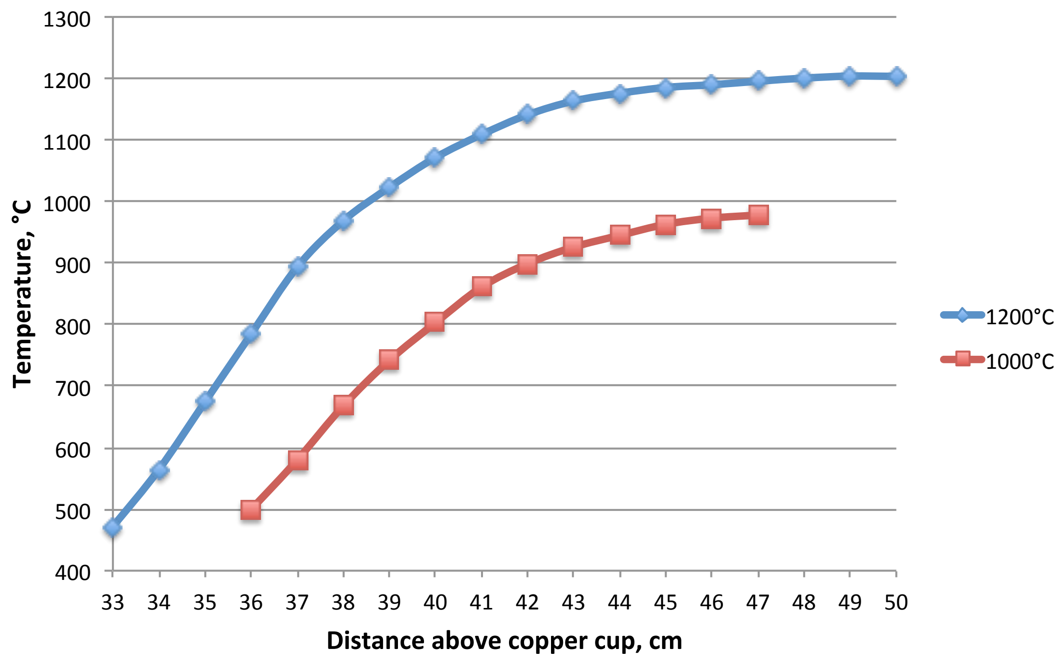

Figure 3.2, Temperature profile for two different furnace temperatures.

3.2.2 Induction furnace

One experiment, the last tabulated in Table 3.1, was performed in an induction furnace. A sketch of the geometric measures in the induction furnace is shown in Figure 3.3. The induction furnace consists of an induction coil made from copper with dimensions as described in the figure. A cylinder of thermally insulating

material, carbon wool, surrounds the load or susceptor, in this case a graphite crucible. High-frequency current goes through the surrounding copper coil and induces electric current in the susceptor.

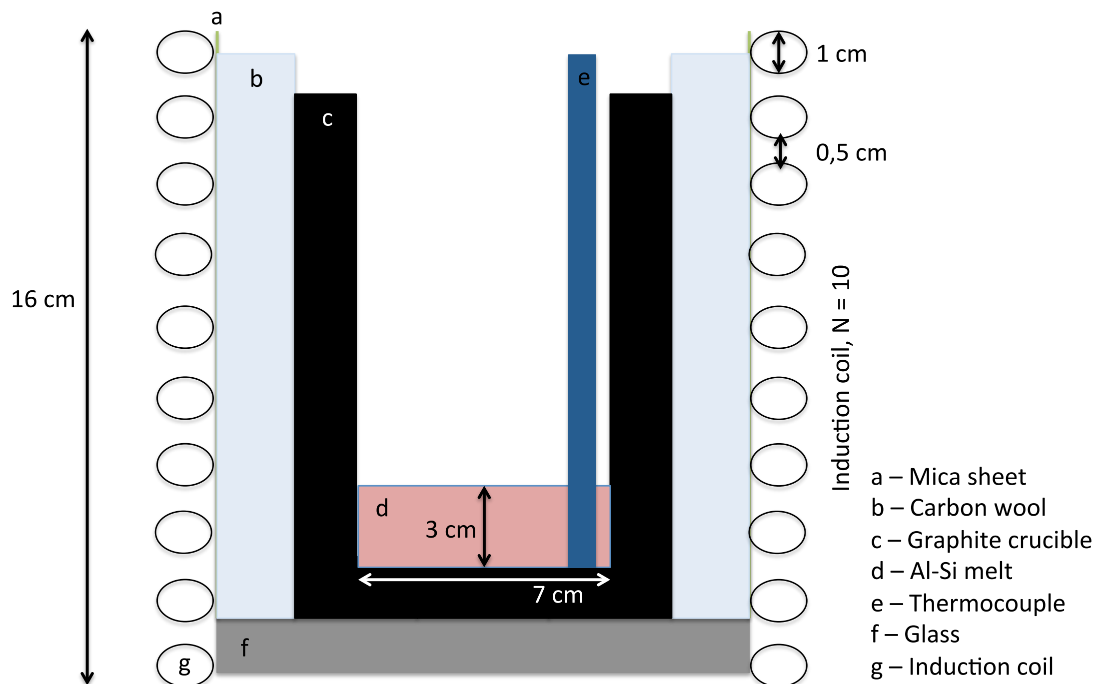

Figure 3.3, Sketch of the geometric measures in the induction furnace. There are 10 induction coils with diameter 1 cm and distance 0,5 cm from each other, whereas the coil length is 16 cm.

The temperature was monitored by a C-type thermocouple placed inside the melt while the heat generating current that was supplied to the furnace were adjusted manually at the power supply control. The furnace was equipped with a rotary pump that gives high vacuum and argon gas was then purged into the furnace until atmospheric pressure was reached. The argon gas was retained to give a flowing atmosphere during the experiment, controlled by a flow meter.

3.3 Materials

Al-18,5wt%Si master alloy provided by Clean Silicon AS were used in experiment DS-1. Analysis of the material is presented in Table A1.1 in Appendix 1. For experiment SGS, a p-type silicon ingot was used. An Al-35wt%Si master alloy

was made in a casting furnace for use in experiments DS-2-3, SG and IH. The addition of aluminium and silicon was found by Equation 3.2 and 3.3.

$$m_{tot} = \frac{m_{Al}}{wt\%Al} \cdot 100 \quad (3.2)$$

$$m_{Si} = m_{tot} - m_{Al} \quad (3.3)$$

1087,7 g Al was melted in the furnace before 585,7 g Si was dissolved in the aluminium to Al-35wt%Si alloy. The casting furnace is an open furnace, which makes the melt available to stir in during the melting. This caused an oxide layer to form in the top of the melt, which was not used in the experiments.

The alloy was cooled with the furnace closed and due to good isolation the cooling rate is relatively slow. The melt solidified from the top and bottom and grew towards the center of the casting. As silicon expands upon solidification, melt was trapped between the moving interfaces and was squeezed out on the top of the casting. [42]

The amount of Al and Si in the alloy was too high for ICP-MS to give a correct analysis. XRF at NTNU was an alternative, but they press the material to pellets so the material must be crushed down to small grains, which was not possible for this alloy as the aluminium makes it soft. XRF at Molab AS was used to analyse Al and Si, as they can analyse directly on a metal piece cut from the material. One piece with a diameter around 3 cm and 0,5 cm in thickness were analysed on each side and the average of these results are given in Table A2.1 in Appendix 2. The sample was analysed on each side due to pores in the material, but it was reported that the analysis results did not differ much from one side to the other.

Selected trace elements were found by ICP-MS analyses. Small pieces were cut out of the master alloy from selected positions (shown in Figure A2.1) and crushed with a mortar to relatively small grains. Two parallels of each metal piece were analysed where each sample around 35 mg material was dissolved in

HF acid. The analysis results are presented in Table A2.2 and Figure A2.2 in Appendix 2.

Mono-crystalline silicon was used as seed in SG and SGS experiments. The material had a <001> orientation.

3.3.1 DS experiments

Quartz crucibles coated with Si_3N_4 was used for the DS experiments, while the alloy were Al-18,5wt%Si for DS-1 and Al-35wt%Si for DS-2-3. The melt binds to the quartz crucible upon solidification as the quartz becomes soft during heating, which is why the coating is necessary. The samples were melted at around 1200°C and held for 2 hours at 47 cm above copper cup to ensure that the material was completely melted. Then the samples were lowered relatively fast to 35 cm or 37 cm above the copper cup, for DS-1 and DS-2-3 respectively (Figure 3.2). The samples were pulled with the desired rate from this position (liquidus temperature) and downwards in the furnace to the solidus temperature, which is shown by temperature measurements in Figure 3.4. DS-1 and DS-2 was pulled with a rate of 0,18mm/min and this can be seen from the figure as the temperature measurements give the same slope. DS-3 was pulled with a rate of 0,12mm/min, and this slope is not as steep as for the other experiments.

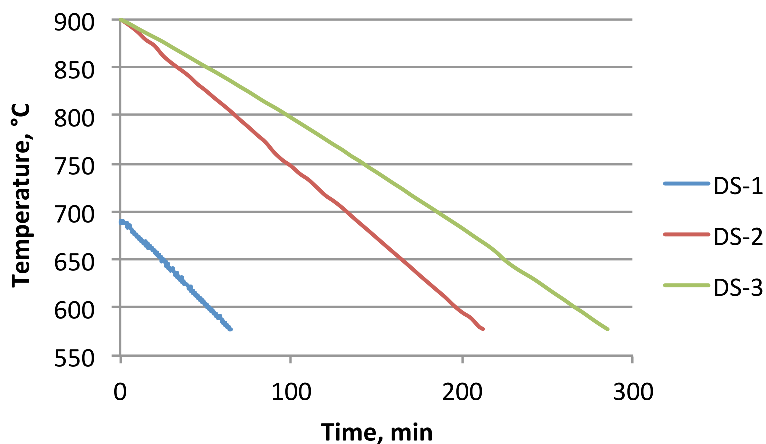

Figure 3.4, Temperature measurements during directional solidification for DS experiments.

3.3.2 SG experiments

Quartz crucibles coated with Si_3N_4 were also used in the SG experiments. For these experiments a mono-crystalline seed were placed in the bottom of the crucible as shown in Figure 3.5a. Silicon has a lower density than the Al-Si melt and to prevent the seed from floating, an alumina stick was used to hold the seed to the bottom of the crucible below the Al-Si melt. The Al-35wt%Si alloy was placed above the seed as shown in Figure 3.5b.

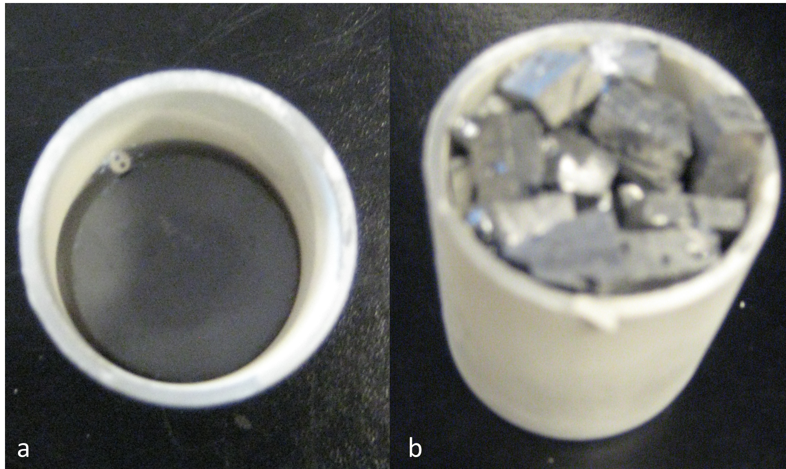

Figure 3.5, Photographs of Si_3N_4 coated quartz crucible with (a) mono-Si seed held by an alumina stick (b) Al-35wt%Si alloy cut into pieces.

The samples were heated to around 900°C and held for 2 hours at 42 cm above the copper cup. It is important that not all the mono-crystalline seed melts down, so the desired amount of melted seed can be used to calculate the final silicon content by Equation 3.4-3.7. This in turn is used to find the appropriate melting temperature by the binary Al-Si phase diagram (Figure 2.12).

$$m_{Si} = m_{Al-Si} \cdot 0{,}35 + m_{melted\ mono-Si} \tag{3.4}$$

$$m_{Al} = m_{Al-Si} \cdot 0{,}65 \tag{3.5}$$

$$m_{tot} = m_{Si} + m_{Al} \tag{3.6}$$

$$wt\%Si = \frac{m_{Si}}{m_{tot}} \tag{3.7}$$

The measured temperature is below the crucible holder. For SG-1 the temperature was measured to 910°C. The top of the seed is approximately 1 cm higher up in the furnace, which will give a temperature increase of 30°C. At 940°C 4,5g of the seed should be melted, while 6g and 6,5g of the seed should melt down in SG-2 and SG-3, respectively at 960°C.

During the experiment the samples were lowered downwards in the furnace with a rate of 0,18 mm/min from liquidus to solidus temperature. Temperature measurements during pulling are shown in Figure 3.6.

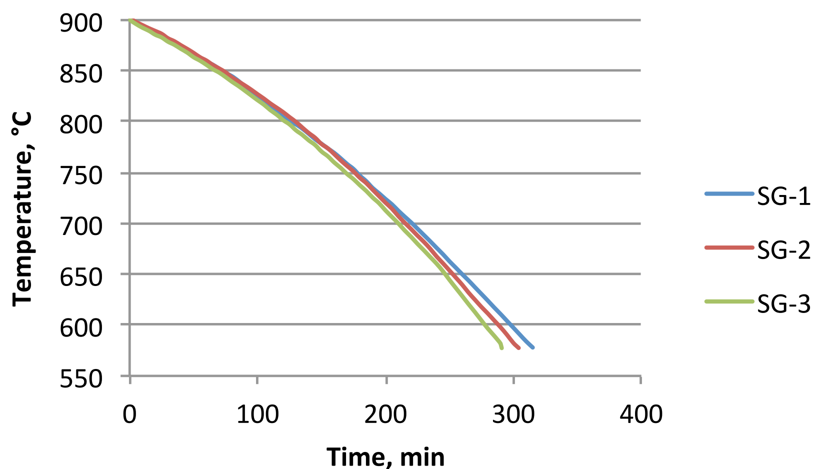

Figure 3.6, Temperature measurements during directional solidification for SG experiments.

The variable in these experiments was the stirring of the melt. For SG-1 there was no stirring, while an alumina tube were turned around in the middle of the melt in SG-2, providing moderate stirring. The material in SG-3 was melted down in a casting furnace at 930°C while a graphite rod was used to stir extensively in the melt. To cool down the sample the power in the casting furnace was turned off, however good isolation provides slow cooling so that the crucible stays intact. The material with the same crucible was then melted down again in the resistance furnace for directional solidification.

3.3.3 SGS experiment

Alumina crucible coated with Si_3N_4 was used for SGS experiment. A mono-crystalline seed were placed in the bottom of the crucible with a silicon ingot on top. As the seed and the ingot is the same material the temperature must be carefully monitored to avoid melt down of the seed, this is also the reason why the seed is higher in this experiment compared to the SG experiments. S-type thermocouples were positioned below the crucible holder and in the melt directly above the seed. The sample was heated to 1407°C and held there for 1 hour before the temperature was increased to 1420°C and held for 10 min. The measured temperatures in the melt during sample pulling are plotted in Figure 3.7.

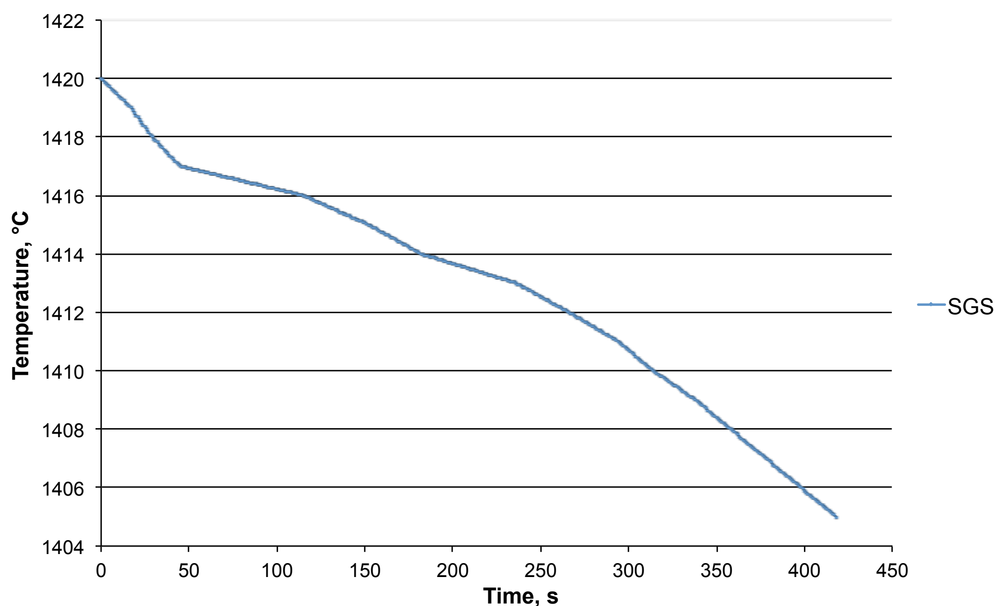

Figure 3.7, Temperature measurements during directional pulling for SGS experiment.

3.3.4 IH experiment

The IH experiment was conducted in an induction furnace. Pieces of Al-35wt%Si alloy were placed in a graphite crucible. The material was heated to 1227°C before cooling was started by manually adjusting the power supply. The temperatures measured in the melt during cooling from liquidus temperature to

solidus temperature are presented in Figure 3.8. The cooling rate was found to 4°C/min.

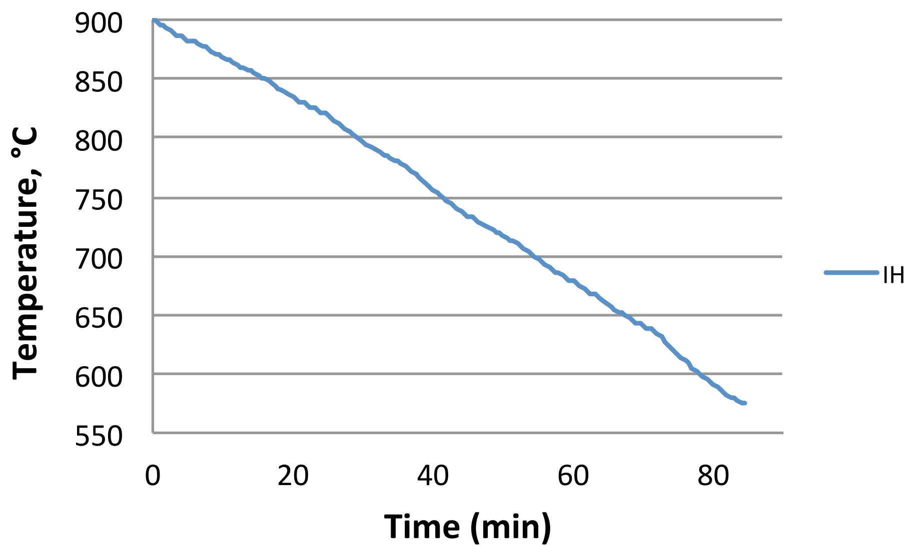

Figure 3.8, Temperature measurements during cooling for IH experiment.

3.3.5 Silicon crystals

A eutectic composition of 12,6wt% Si in the Al-Si system gives a theoretical maximum percentage of primary silicon in the material of 6,75wt% when the alloy contains 18,5wt%Si and 25,63wt% when the alloy contains 35wt%Si. These values are calculated by the lever rule, shown by Equation 3.8 and 3.9.

$$\frac{18,5wt\% - 12,6wt\%}{100wt\% - 12,6wt\%} = 6,75wt\% \qquad (3.8)$$

$$\frac{35wt\% - 12,6wt\%}{100wt\% - 12,6wt\%} = 25,63wt\% \qquad (3.9)$$

3.4 Analysing techniques

Mainly microscopes are used to analyse the samples. Light microscopy was used on the major part of the samples, while electron microscopy were used to find grain distribution and orientation. EPMA were used to find aluminium contamination.

3.4.1 Mechanical preparation of the samples

Before the samples were analysed by light and electron microscopy they were cut to expose the vertical cross-section except SGS that was cut 1 cm above the seed to expose the horizontal cross-section. The cross-sections were then ground with SiC papers (mesh 80 to 4000) and polished with diamond paste of 6-1μm. Then they was cleaned with water, soap and ethanol and dried in hot air. Samples from SG experiments was in addition cut into smaller pieces, moulded into resin and then prepared mechanically as described above before submitted to micro probe analyses.

3.4.2 Analysis of silicon crystals by light microscopy

The cross-section of DS and SG samples was captured with a light microscope. Leica MEF4M light microscope was used to capture images of DS-1 and DS-2 with 2,5X magnification. Each image was put together to form the entire cross-section, this is shown for sample DS-1 in Appendix 3. For DS-3 and SG samples Leica REICHERT MeF3A light microscope was used to capture images. This microscope has a program that automatically moves the samples and takes pictures with 2,5X magnification. However, the metal plate below the sample must have a diameter of 34 mm. This means that there are some areas on the sides of the samples that are not captured. These areas were captured with Leica MEF4M. The IH sample has a large cross-section, which is why the cross-section was scanned for further analysis.

The microscope images are then analysed with ImageAccess EasyLab to measure crystal area and length of the crystals. However, the program requires good contrast, which was not achieved on the captured images. Colouring the primary silicon crystals using Paint.NET gave the required contrast. To get the crystal length, a linear function was used to draw a line equal to the length of the crystal. The crystal area was found by using the Phase fraction under the Phase Analysis function, which distinguishes between three phases: the area around the sample, the Si-Al eutectic phase and the primary crystal phase. The purpose of these analyses was to get quantitative results of the primary Si crystals to get a better understanding of the crystal growth with respect to size and position.

3.4.3 Electron probe micro-analyser (EPMA)

Element analyses were carried out on the seed-alloy interface for SG samples by employing EPMA. This equipment is basically a scanning electron microscope designed and optimized for X-ray analysis of elements from very small areas. [24] The purpose was to investigate whether the mono-Si and Si primary crystals were contaminated with Al.

3.4.4 Electron backscatter diffraction (EBSD)

EBSD is a detector on the electron microscope that provides quantitative microstructural information about the crystallographic nature of the material. As the phase and orientation at each pixel in the map is known it differs from conventional SEM and give additional visual and analytical information. Inverse pole figure (IPF) orientation component uses a basic RGB colouring scheme, fit to an inverse pole figure. For cubic phases, full red, green and blue are assigned to grains whose <100>, <110> or <111> axes, respectively, are parallel to the projection direction of the IPF (typically, the surface-normal direction). Intermediate orientations are coloured by an RGB mixture of the primary components. [43] The SGS sample was cut around 1 cm above the seed-metal interface, to give a horizontal cross section and analysed by EBSD to investigate the grain distribution and grain orientation.

4 Results

Results for the eight experiments conducted are presented in this section. For DS experiments, pulling rate for directional solidification and silicon content was looked upon to optimise the growth of silicon crystals. Further, the use of seeded growth with the effect of stirring in the melt was investigated in the SG experiments. The experiments mentioned in the previous section are presented with images of vertical cross-section and analysis of primary silicon crystal area and length of crystals. In addition, results from EPMA are given for the SG samples.

To investigate whether seeded growth were possible for pure silicon, this was conducted in experiment SGS and are presented by EBSD analysis, which shows the grain distribution and orientation in the horizontal cross-section. The experiment conducted in the induction furnace, named IH, is presented with analysis of primary silicon crystal area in different areas of the sample in the vertical cross-section.

4.1 Position and size of primary Si crystals in DS and SG experiments

Images of vertical cross-section of samples from DS and SG experiments are presented in Figure 4.1. Oxide layers formed in the top of the melt, preventing the material in the top of the sample to melt down properly. The primary silicon crystal area was found in three parts of the samples; top, center and bottom. These analyses were found to give the best presentation of occurrence of primary Si crystals in the cross-section, as the different areas can be compared. The results from these analyses are given in percentage and written together with the images of cross-section for each sample in Figure 4.1.

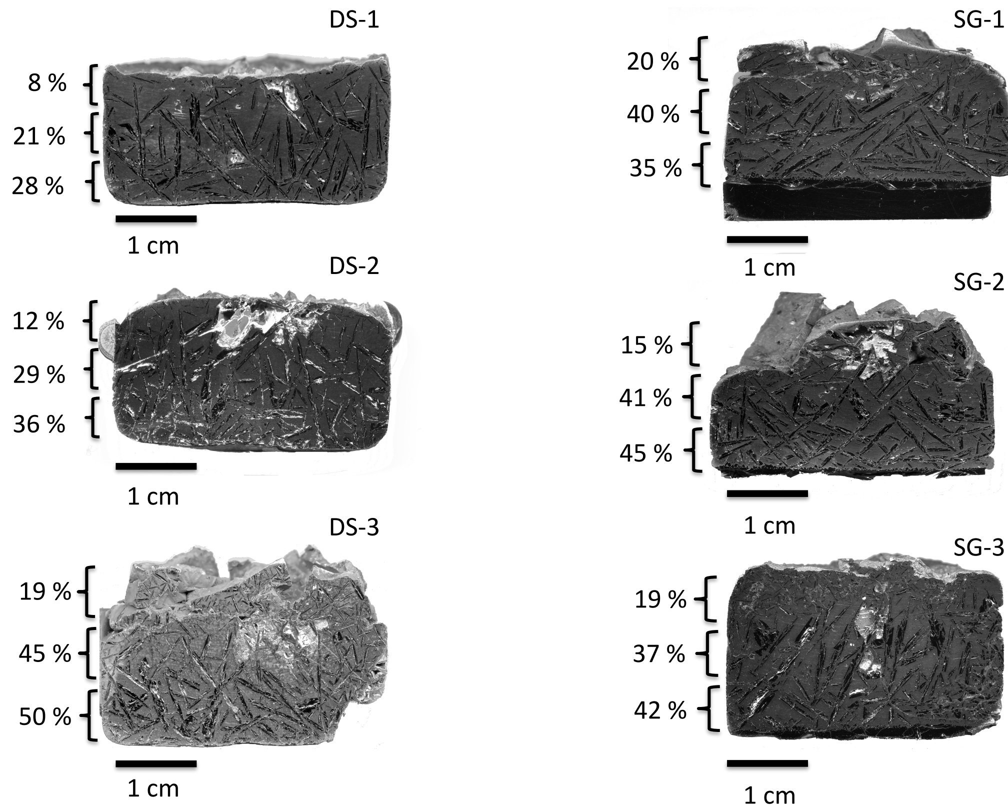

Figure 4.1, Primary Si crystal area shown at the respective areas for the different samples in DS and SG experiments.

The results show that the sample from experiment DS-1 has a lower percentage of crystal area compared to the other samples, which is expected as this sample has lower silicon content in the starting material. For samples from experiment DS-2-3 and SG, the percentages differ from each other in some degree. However, there is a general trend that the occurrence of Si crystal is high in the bottom of the sample and decline further up.

Analyses on crystal area give information on the position of the Si crystals, which is why crystal length are also analysed to get more information regarding the size of the crystals. The shape of the silicon crystals was found to primarily have rod-like morphology in the cross-section. This is why the length of the crystals is selected to give more information about the crystal size as the length of the rods give information on how large the crystal is. The number and length of Si crystals in the cross-section are presented in Figure 4.2 and 4.3 for each experiment.

Figure 4.2 presents the total number of crystals in the samples together with number of crystals in the length intervals.

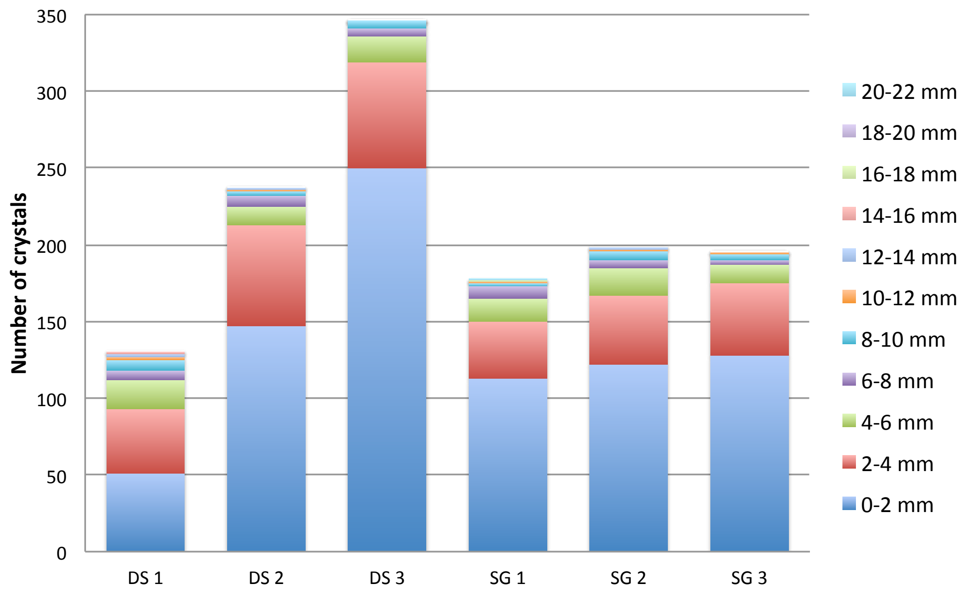

Figure 4.2, Number of crystals together with crystal length in the cross-section for DS and SG experiments.

Most of the crystals have a size smaller than 6 mm, which is why crystals with a size larger than 6mm are shown in Figure 4.3 to give a better presentation.

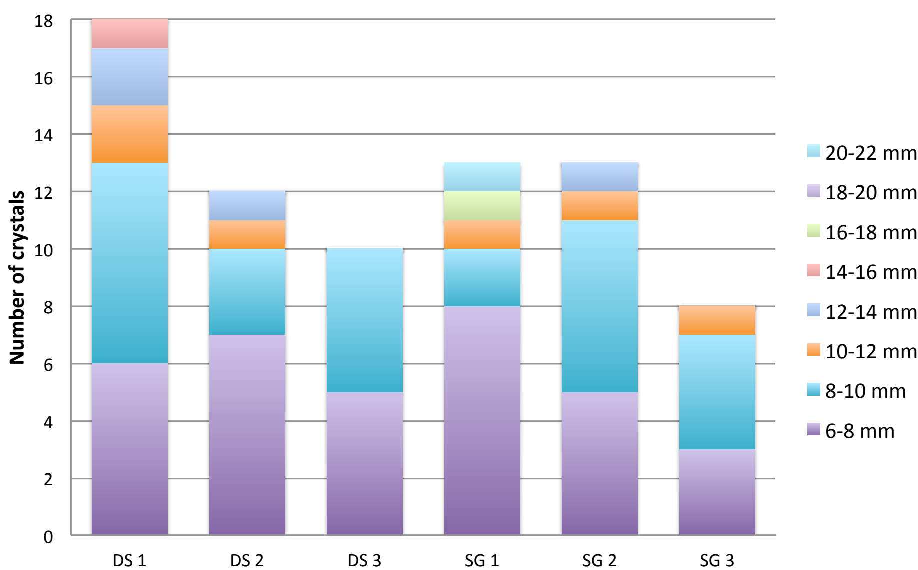

Figure 4.3, Number of crystals and crystal length for crystals larger than 6 mm in cross-section for DS and SG experiments.

4.2 Aluminium contamination in seed and primary Si crystals

To investigate whether the mono-crystalline seed and primary Si crystals in SG experiments were contaminated with aluminium, EPMA analyses were carried out. Analysis of elements was performed on three positions in each sample, shown by SG-1 as an example in Figure 4.4.

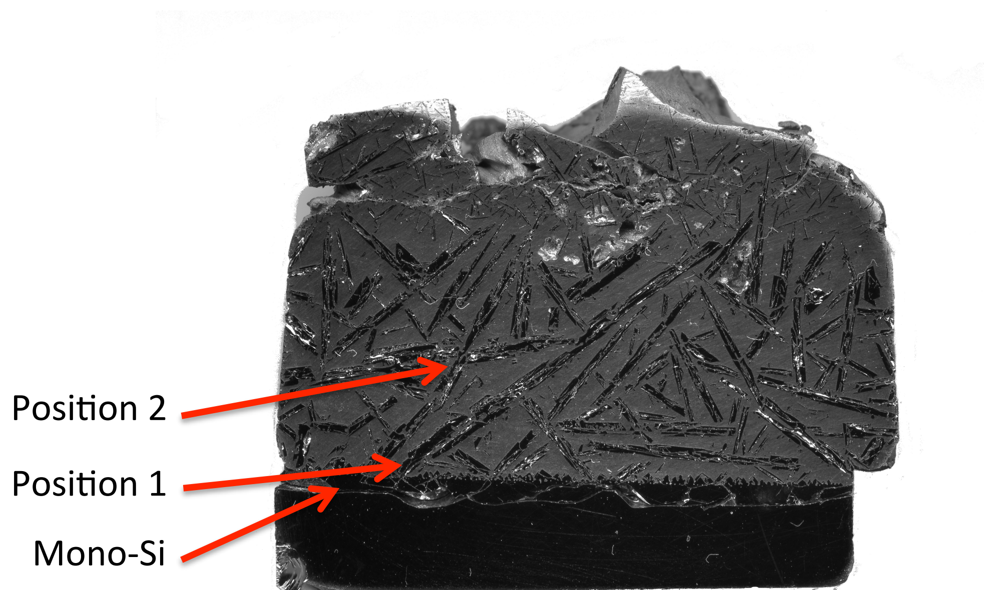

Figure 4.4, The cross-section of SG-1 show the three positions analysed on with EPMA.

Figure 4.5 shows the plotted results from the EPMA analyses. Each experiment was represented with two samples and it were analysed on elements in three areas in each position. The graphs on the left hand are the silicon content in these three positions shown in blue, while the graphs on the right hand are the aluminium content in two positions shown in red. There is no graph for the aluminium content in mono-Si as the detected aluminium was under the detection limit. Also iron was detected in the samples, however the amount was under the detection limit for all samples and is neglected.

High silicon content is detected for all samples, but especially for samples from experiment SG-3. As mentioned no Al are found in mono-Si for all samples while

it was detected in position 1 and 2. The Al content was lower in samples from experiment SG-3 compared to the others.

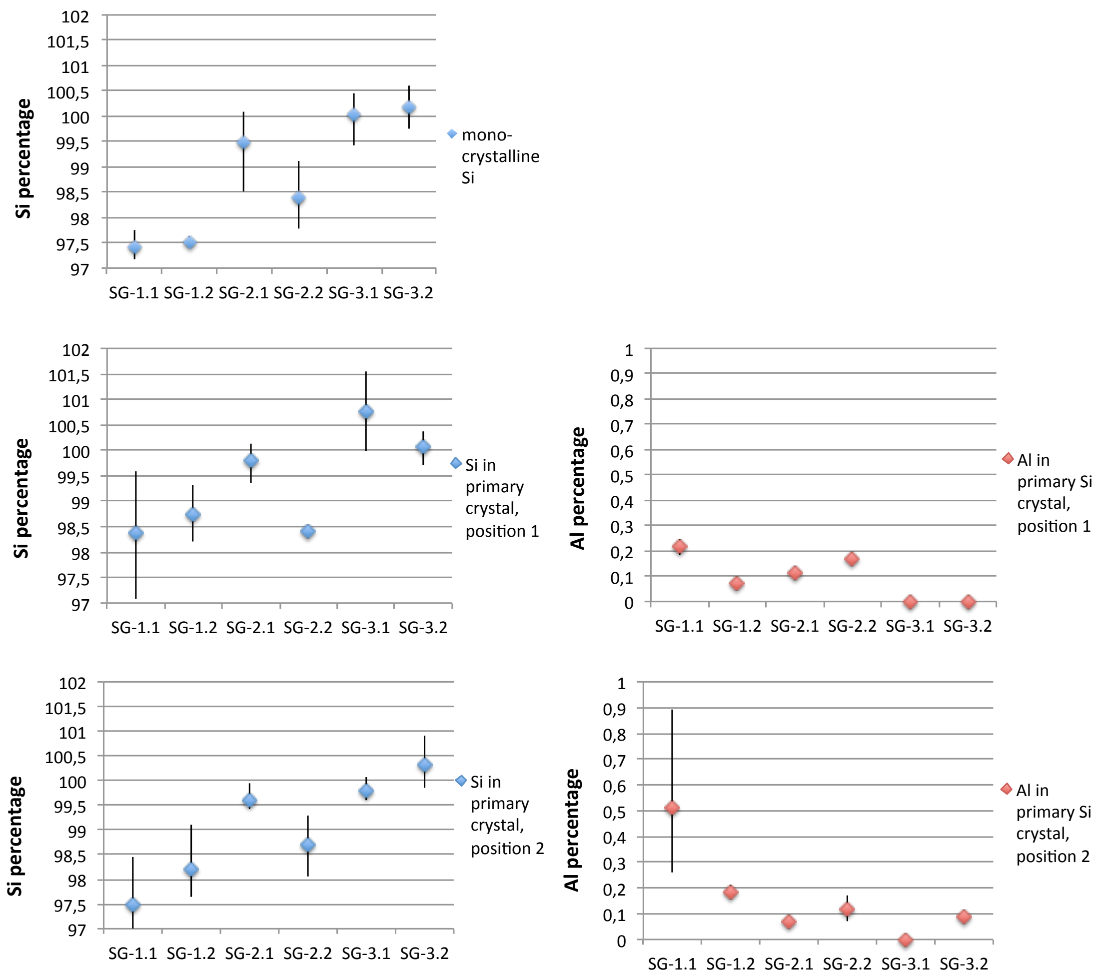

Figure 4.5, Plotted results from EPMA analyses in samples from SG experiments. Three graphs on the left give Si content for three different positions while graphs on the right give Al content in Si for position 1 and 2. The error bars specify the given positive and negative deviations for each sample, which for some points are small and do not appear.

4.3 Position of Si primary crystals after electromagnetic separation

Cross-section of sample from IH experiment was scanned and analysed to get information about the crystal position in the melt. The scanned cross-section is viewed in Figure 4.6. The primary silicon crystal area was found in four parts of the sample; top, middle, right and left, divided by blue dotted lines in Figure 4.6.

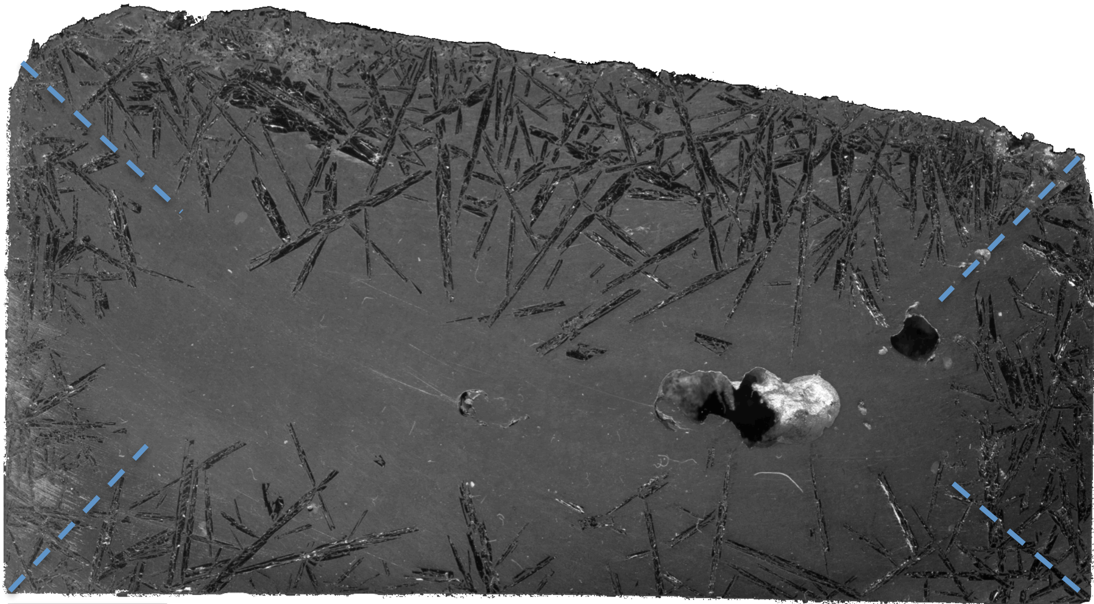

Figure 4.6, Scanned image of cross-section from experiment IH. Blue dotted lines shows where the different parts are separated.

The crystal area for the entire sample along with the different parts is given in Figure 4.7.

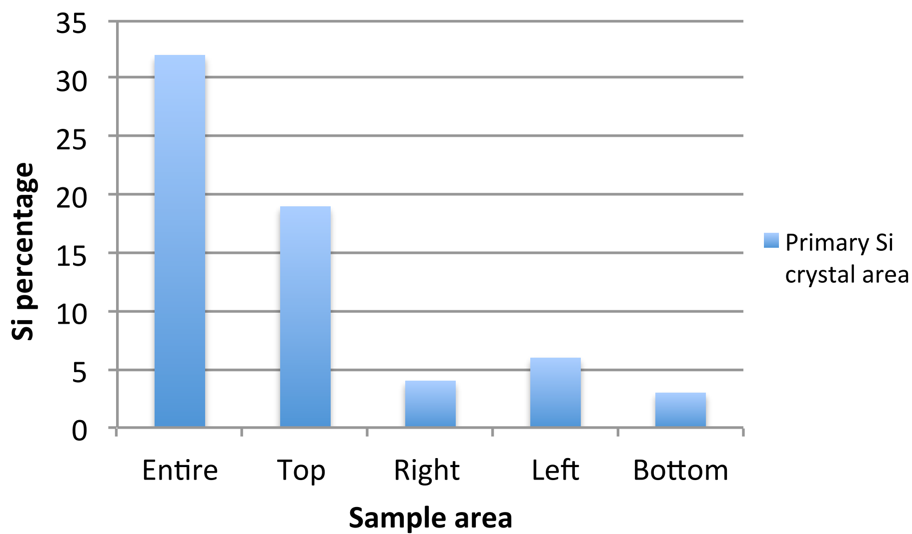

Figure 4.7, Results from primary Si crystal area analysis on experiment IH for entire sample and for the four parts; top, right, left and bottom.

4.4 Si crystal growth from seed without aluminium

Experiment SGS was conducted to investigate whether silicon material without aluminium could grow from a mono-crystalline seed. The crystal distribution shown in Figure 4.8 is found by EBSD from the horizontal cross-section of the sample around 1 cm over the seed. It can be seen that a large single crystal have grown in the middle of the ingot, shown by an orange colour. Other, smaller crystals are seen in the sides of the sample and are shown by various colours.

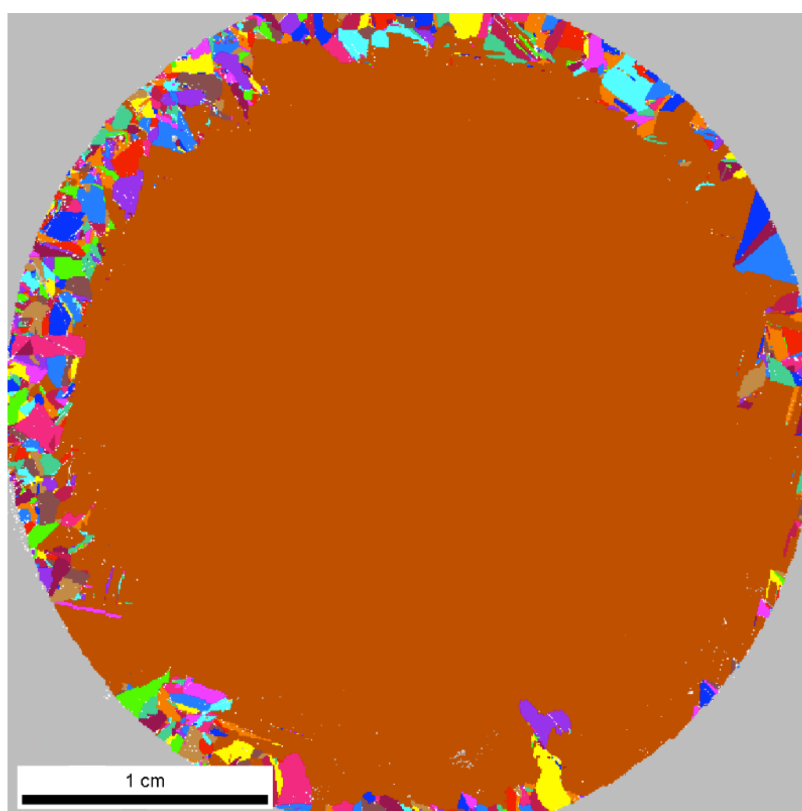

Figure 4.8, Crystal distribution in the horizontal cross section for SGS experiment found by EBSD.

Finding the crystal orientation by EBSD with IPF can verify if the single crystal in the silicon material are grown from the seed. The IPF result is shown in Figure 4.9a, which is taken at the same cross-section as the crystal distribution. The inverse pole figure, shown in Figure 4.9b, shows that a red colour represents the <001> orientation. From the sample it can be seen that the single crystal has a red colour. This means that the crystal has a <001> orientation, which is the same orientation as the seed and proves that the silicon material has grown from

the seed. On the sides there are different small grains with different orientations shown by various colours.

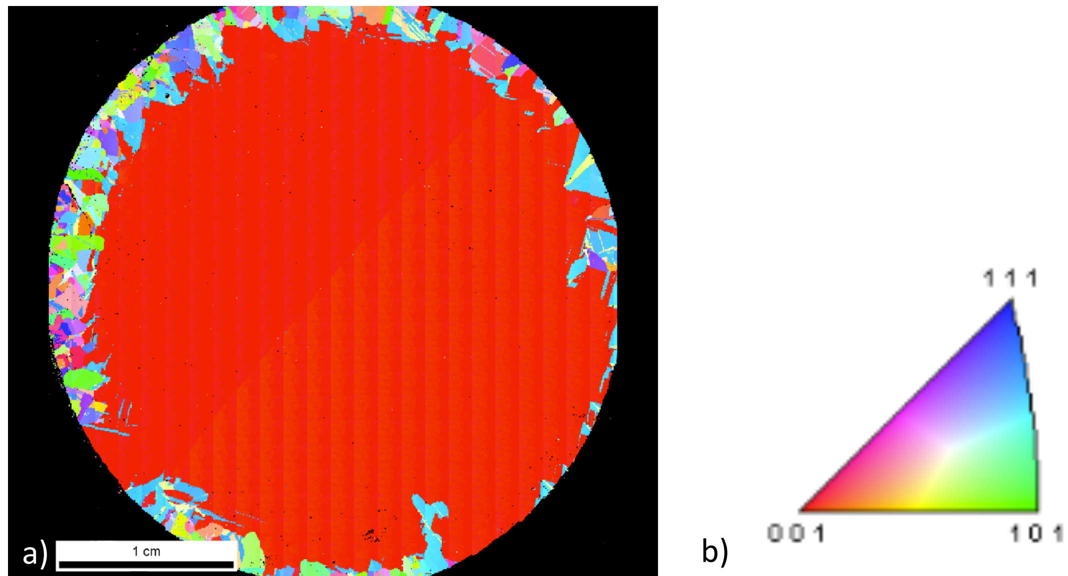

Figure 4.9, a) Crystal orientation in the horizontal cross-section for SGS experiment b) Inverse pole figure.

5 Discussion

The analysis of the starting material showed higher silicon content than 35wt%Si, and this will be discussed. The position of the Si crystals in the samples solidified by directional solidification was not as distinct and the crystal size was not as large as expected and will be compared with literature findings. The crystal area found in DS and SG samples is larger than what is possible according to theoretical calculations, so the probable reasons for this are discussed.

Crystal area and size of crystals will be compared among the experiments conducted and the parameters varied are looked upon to get an understanding of the differences in the results. Seed was applied to SG experiments and it was expected that the silicon crystal growth would increase because of this. This was not the case and contamination of the seed together with melting of the seed is studied to find an explanation for the growth behaviour.

The separation of Si crystals by electromagnetic force was not successful as silicon crystals were found in all sides of the melt, and not only in the vicinity of the crucible wall as was expected. The Si separation is compared with literature findings, as there are no parallel experiments conducted on this experiment type.

5.1 Analysis of the 35wt%Si master alloy

The Al-35wt%Si master alloy were analysed by XRF to 46,1wt%Si. One piece of alloy from the central part of the alloy ingot were analysed on both sides. It is believed that these results are correct, as they did not differ much from one side to the other. 585,7g Si and 1087,7g Al were melted together under stirring of the melt, which means that the alloy should have a final composition of 35wt%Si. As higher silicon content is reported from the analysis it is believed that the overall silicon content for the entire alloy material is 35wt%Si but that the silicon is distributed unevenly. For the experiments, small pieces of master alloy material were cut from different parts of the ingot to minimise the uneven distribution.

The Al-35wt%Si alloy was analysed by ICP-MS. Selected trace elements was analysed on and the results are given in Appendix 2. The distribution of phosphorus deviates from the other values in point 5 and 7. Point 5 is the melt that was squeezed to the top during solidification while point 7 is at the side of the ingot in the lower end. The average phosphorus content is 7,15 ppm. The boron content is generally higher in the middle of the ingot than at the top and side and has an average of 9,05ppm.

The dominating contamination in the material was iron with an average of 3931ppm. Na and Ca had an uneven distribution in the ingot while the other elements seems to be well distributed based on the analysis.

The starting material contained impurities, because it was desirable to investigate the growth behaviour under conditions close to an actual refining process.

5.2 Pulling rate during directional solidification

The pulling rate during directional solidification is important for the shape of the solid-liquid interface. During the directional solidification the pulling rate for DS-1-2 and SG experiments were 0,18mm/min while a slower pulling rate of 0,12 mm/min was used in experiment DS-3. The temperature measurements show a linear decrease in the cooling rate for all DS and SG experiments.

For experiment SGS, a fast pulling rate of 4,8 mm/min were used. The temperature measurements for SGS were measured just above the seed during the pulling, shown in Figure 3.7. The measured temperature has a stagnation at 1417°C and 1414°C. This can indicate a phase transformation from liquid to solid. It is however not easy to say at which temperature the phase transformation occur from this temperature curve, but the literature claims that the silicon has a melting point at 1414°C [11].

When directional solidification is carried out the growth conditions that may cause the interface to break up from planar to cellular, as mentioned in section 2.2.4, are the solidification velocity, temperature gradients in the melt and impurity concentrations. If the solid-liquid interface breaks up and columnar cells start to grow, both grain size and impurity distribution will be largely influenced. [24] These are important factors for the refining, which is why the pulling rate and temperature gradient are calculated for all directional solidification experiments and presented in Table 5.1. These values are then found in Figure 5.1 where they are used to read off the solidification morphologies.

Table 5.1, Microstructures according to cooling rate.

Experiment	Pulling rate, V (m/s)	Temperature gradient, G (K/m)	Cooling rate, $\dot{T}$ (K/s)	Microstructure according to Figure 2.8
DS-1	$3 \cdot 10^{-6}$	9508	0,029	Columnar dendrites
DS-2	$3 \cdot 10^{-6}$	8464	0,025	Columnar dendrites
DS-3	$2 \cdot 10^{-6}$	9491	0,019	Columnar dendrites
SG-1	$3 \cdot 10^{-6}$	5599	0,017	Columnar dendrites
SG-2	$3 \cdot 10^{-6}$	5510	0,017	Columnar dendrites
SG-3	$3 \cdot 10^{-6}$	5680	0,017	Columnar dendrites
SGS	$8 \cdot 10^{-5}$	300	0,024	Columnar dendrites

Table 5.1 shows that the microstructures in all samples are expected to be columnar dendrites. The cooling rate is largely influenced by the temperature gradient in the resistance furnace that was presented in Figure 3.2. As the

samples were pulled downward in the furnace, DS experiments were solidified in a larger temperature gradient compared to SG experiments, which can be seen from the cooling rate. The reason why DS-3 has a lower cooling rate than DS-1-2 is because of the slow pulling rate.

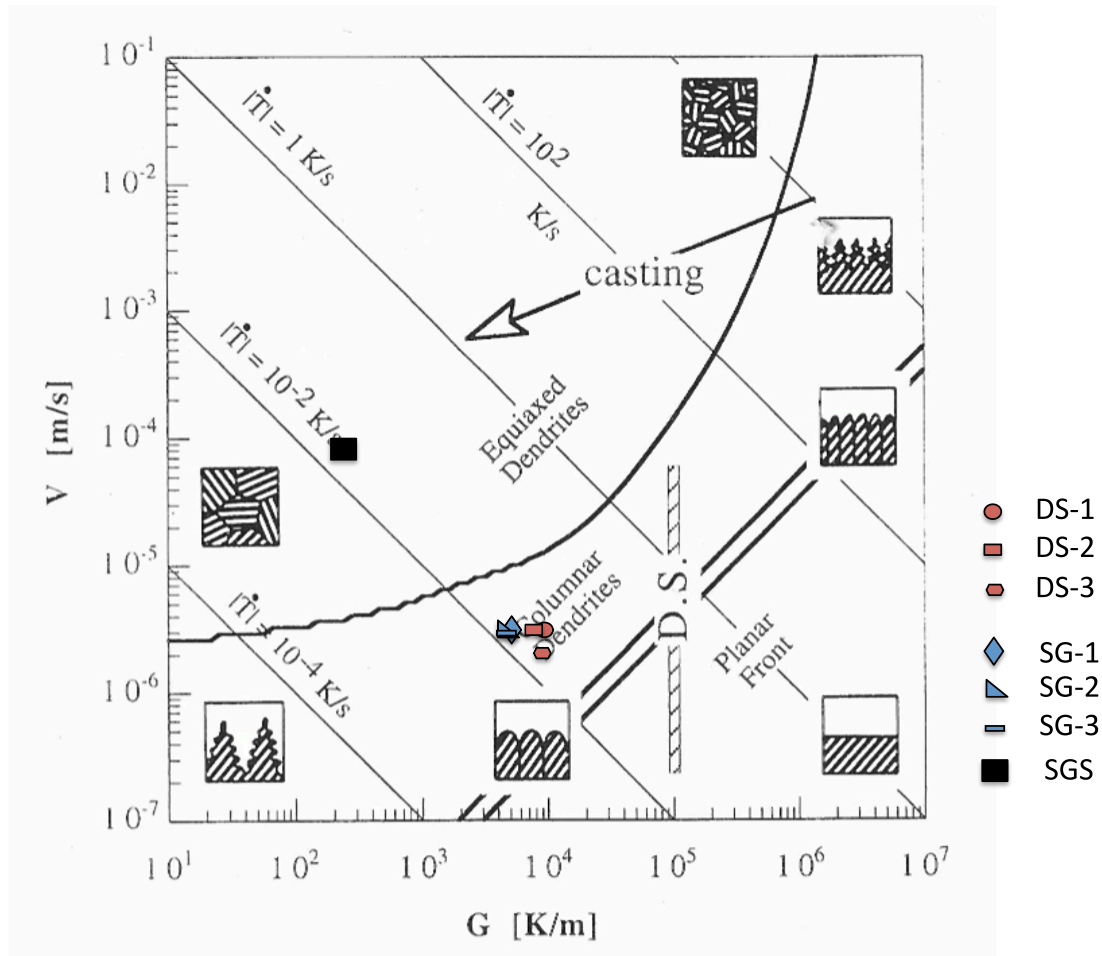

Figure 5.1, Solidification morphologies for the DS, SG and SGS experiments from values shown in Table 5.1. DS experiments are shown in red. SG experiments are shown in blue, the values are not very different from each other so the points overlap. SGS experiment is shown in black.

To obtain a planar front with the temperature gradient in the resistance furnace a pulling rate of 0,012 mm/min are required if Figure 5.1 are to be followed. However, a single crystal was grown in experiment SGS, which is said to be columnar dendrites according to Figure 5.1.

The temperature gradient is lower for experiment SGS than for the rest of the experiments. This is because the directional solidification for Al-Si melts must go

from liquidus to solidus line, which is a temperature region of 900°C - 577°C for 35wt%Si melt and 670°C - 577°C for 18,5wt%Si melt. As SGS only contains silicon, the directional solidification most go from above to below the melting temperature, giving a lower temperature gradient.

5.3 Growth rate of Si crystals

Equations for growth rate are presented in the theory under section 2.2.2. The equations are only valid if the growth rate is assumed to be diffusion controlled. Calculation of the critical growth rate for Al-35wt%Si alloy are done at a temperature of 900°C (liquidus curve). The critical growth rate, V_C, at 900°C is expressed by Equation 5.1 with $\partial X_{Si\ in\ Si-Al\ melt}/\partial T = 0{,}0011$ and $D_{Si\ in\ Si\text{-}Al\ melt} = 1{,}8 \cdot 10^{-8}\ m^2/s$. The equation is valid when the Al-Si alloy is placed in a temperature gradient, $\partial T/\partial x$ (K/m). [22]

$$V_C = 1{,}98 \cdot 10^{-11} \frac{\partial T}{\partial x} \tag{5.1}$$

The critical growth rate is calculated for samples solidified directionally with 35wt%Si alloy and are presented in Table 5.2.

Table 5.2, Critical growth rate for experiments containing Al-Si alloy solidified directionally.

Experiment	Critical growth rate (m/s)
DS-2	$1{,}7 \cdot 10^{-7}$
DS-3	$1{,}9 \cdot 10^{-7}$
SG-1	$1{,}1 \cdot 10^{-7}$
SG-2	$1{,}1 \cdot 10^{-7}$
SG-3	$1{,}1 \cdot 10^{-7}$

If the critical growth rate of Si from Al-Si melt is to be compared with Si growth rate, at the order of 10^{-5} (m/s), during directional solidification in the metallurgical refining process for Si, it can be seen that the critical growth rate from Table 5.2 are much smaller. Thus, bulk Si growth is unrealistic for an actual

refining process with Al-Si melt. Therefor, removal of the eutectic phase between the primary Si crystals by acid leaching is necessary to collect the Si crystals from the material. [22] A microscope image from experiment DS-1 are shown as an example in Figure 5.2, where the eutectic phase is found between the primary Si crystals.

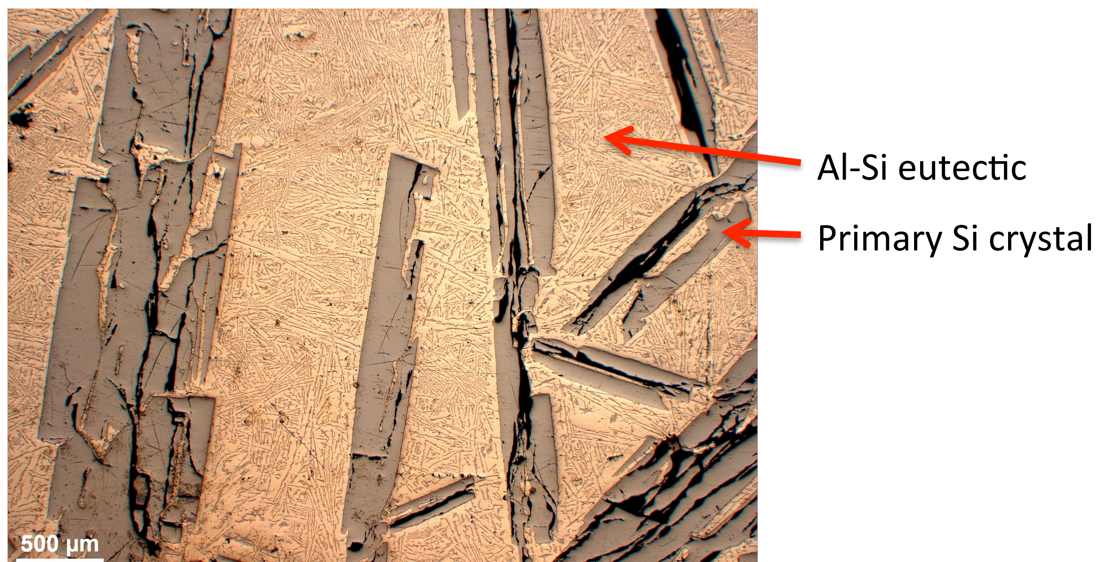

Figure 5.2, Microscope image with 2,5X magnification from experiment DS-1 where the eutectic phase and primary Si crystals are pointed out.

5.4 Positioning and size of the primary Si crystals by directional solidification

Three experiments were conducted for solidification of Al-Si melt by directional solidification and for solidification of Al-Si melt with seed by directional solidification. Pulling rate and silicon content are varied under directional solidification without seed, while stirring in the melt are varied under directional solidification with the use of seed. Thus, the uncertainty of the amount and agglomeration of the primary Si crystals in the cross-section of the sample is unknown, as there are no parallel experiments conducted.

5.4.1 Effect of temperature gradient and cooling rate

Nishi and co-workers [7] investigated the growth of Si crystals by directional solidification from a Si-55,3at%Al melt. Their purpose was to obtain bulk silicon crystals from the Al-Si melt and this was investigated by varying temperature gradient and cooling rate for the directional solidification. The six experiments are shown in Figure 5.3. In sample (c) and (f) the crystal-melt interface is classified as flat and no melt remnant were found in the successfully obtained bulk Si crystals.

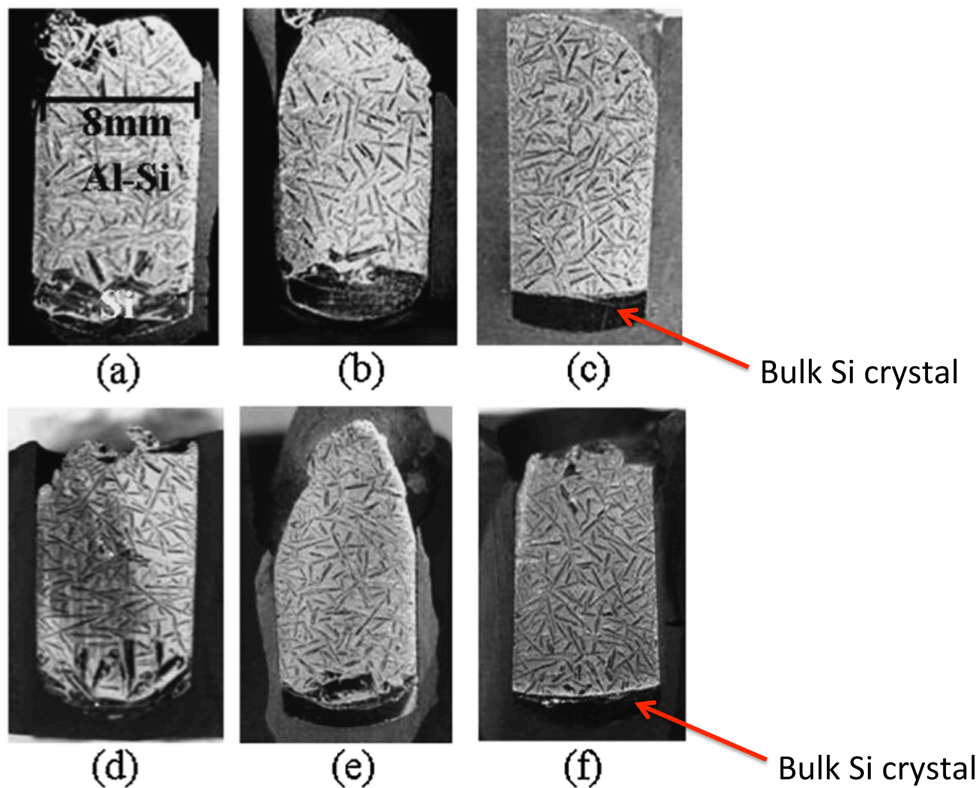

Figure 5.3, Photographs of cross-section of samples solidified directionally by Nishi et al. The appropriate conditions were used in (c) and (f) as bulk Si crystals were grown. Modified from [7]

It was expected that the growth of Si crystals from the Al-Si melt in the experiments conducted in this thesis would be similar to the ones shown in Figure 5.3. To compare the results more in detail, the various temperature gradients and cooling rates used in the experiments are presented in Table 5.3 together with experiments conducted in this thesis. Both the temperature gradient and the cooling rate are lower in the experiments conducted by Nishi and co-workers. Miyahara and co-workers [20] found that the average grain size of silicon crystals decreases as the solidification velocity increases. Figure 4.1.

show the cross-sections of DS and SG experiments. The crystals are not as large as the crystals shown in Figure 5.3 (a) and (d) and there is no indication of bulk Si growth in the lower part of the samples.

Table 5.3, Comparison of temperature gradient (K/mm) and cooling rate (K/min) for experiments conducted in this thesis and experiments done by Nishi et al.

Experiment	Temperature gradient (K/mm)	Cooling rate (K/min)	Experiment (Nishi et al.)	Temperature gradient (K/mm)	Cooling rate (K/min)
DS-1	9,5	1,74	(a)	1,5	0,105
DS-2	8,5	1,50	(b)	1,5	0,084
DS-3	9,5	1,14	(c)	1,5	0,031
SG-1	5,6	1,02	(d)	4,0	0,273
SG-2	5,5	1,02	(e)	4,0	0,194
SG-3	5,7	1,02	(f)	4,0	0,08

The silicon content in the material used by Nishi and co-workers were higher than what was used in DS and SG experiments conducted in this thesis. It is reported in the literature that the silicon crystals will be both longer and thicker with increasing silicon content. [9] However, this can not be the only reason for the difference in size as the silicon crystals are that much smaller in DS and SG experiments compared to experiments (a)-(f).

Nishi and co-workers had samples with a smaller diameter and used graphite crucibles not quartz crucibles. The argon gas flowing in the furnace during the experiments was purified and dried and prevented formation of oxides in the melt, which was not the case for DS and SG experiments and could only have a small influence on the crystal growth. Thus, it is concluded that the temperature gradient and cooling rate would essentially determine size and position of Si crystals.

5.4.2 Si crystal area in cross-section compared to theoretical calculations

The area of the crystals covers a larger percentage of the cross-section than what is possible according to theoretical calculations in both DS and SG samples. The maximum percentage of Si crystals in the entire sample is calculated to 6,75% for the starting material that contains 18,5wt%Si and 25,63wt% for the starting material that contains 35wt%Si.

The crystal area is found from the cross-section of the sample, meaning that the surface analysed on are from the central part of the ingot. One possible explanation for the high crystal area is that it varies within the ingot. This can indicate that there is more crystal growth in the central part of the ingot compared to on the sides.

For samples with starting material containing 35wt%Si the silicon distribution is uneven as previously discussed. However, this alone cannot explain the high crystal area as it occurs in all samples. If the silicon content are higher in some samples it has to be less in others as the average of the master alloy is believed to contain 35wt%Si.

5.4.3 Morphology of Si crystals

The primary Si crystals grown from sample with 18,5wt%Si was expected to have a fish-bone or star-like morphology as is reported for samples around this silicon content. [9] However, it can be seen from Figure 4.1 that the Si crystals has a rod-like shape. It is expected that these rods in realty are plate-like structures, but this is not observed since the crystals not are collected from the melt. Experiments with 35wt%Si are supported by the literature to have plate-like Si crystal growth, [9] which are found in DS-2 and shown in Figure 5.4. Because of these plates, all rod-shaped crystals in the cross-sections are expected to be plate-like Si crystals.

Figure 5.4, Plate-like morphology of primary Si crystals shown by sample DS-2.

5.4.4 Pulling rate and silicon content

Findings in DS experiments by variation in silicon content and pulling rate were used further in SG experiments. The Si crystals is found to cover a larger area of the cross-section in samples with 35wt%Si compared to sample with lower silicon content. This is in accordance with the theory, which is why starting material with 35wt%Si was used in the following experiments. Decrease in the pulling rate were performed for DS-3 and compared to DS-2 it was found an increase in the crystal area and decrease in crystal size. Even though the crystal area increased with decreasing pulling rate, the increase in crystal area are not big enough considering the higher amount of energy used during slow pulling. This is why pulling rate of 0.18mm/min was selected for SG experiments.

5.4.5 Position of Si primary crystals by directional solidification

The Si crystal area is highest in the lower part of the sample and decreases further up. This is caused by the directional solidification, as the ingot is pulled downward in the furnace. The silicon will start to grow upwards from the bottom of the ingot as it holds a lower temperature than the rest of the material. There is higher availability on silicon atoms in the beginning of the solidification and more silicon growth will occur in the lower part.

As the master alloy used in DS-2-3 and SG experiments have a silicon content of 35wt% these are compared and shown in Figure 5.5. The lines show the average crystal area for upper, central and lower region as well as the calculated maximum crystal area for the whole sample. The deviation from the average crystal area is shown with points for the different experiments in the respective regions.

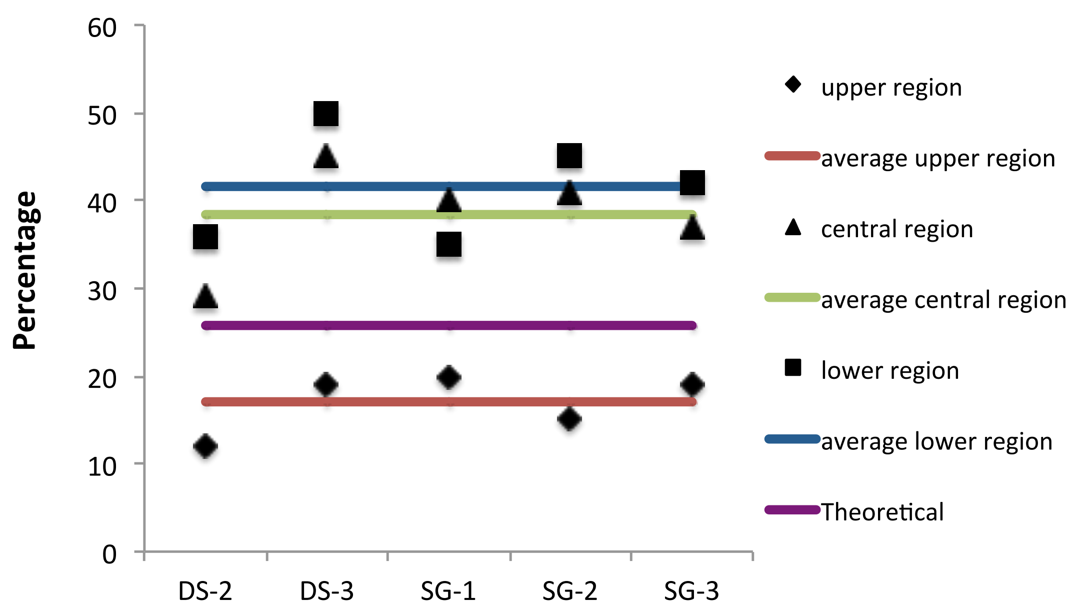

Figure 5.5, Plotted datas of crystal area in percentage for all samples containing 35wt%Si from DS-2-3 and SG experiments.

Experiment DS-2 and DS-3 deviates more from the average crystal area than the SG experiments. Compared to the average values, DS-2 has a lower crystal area in all regions while DS-3 has a higher crystal area in all regions. Since the master alloy is found to have an uneven distribution of silicon it might be that the material used in DS-2 have a lower silicon content than 35wt% while the material used in DS-3 have a higher silicon content.

Pulling rate for DS-3 is slower than what is used in the other experiments. This can also affect the crystal area as the silicon crystals have longer time to grow before the material solidifies.

It was expected that the seed positioned in the bottom of the crucible in the SG experiments would act as nucleation center, and cause a higher fraction of silicon crystals to occur in the lower part of the melt. This is because the solution nucleates more readily during secondary nucleation, which is when crystals of the solute are added to the melt. [13] As the crystal area in SG experiments did not deviate much from experiment DS-2-3, it was concluded that the silicon crystals did not grow from the seed.

The SG experiments have a similar crystal area if summarised, while the distribution in the different regions varies. SG-1 has a higher crystal area in the central region compared to the lower region. This is not expected, however the difference is 5% and can be caused by uncertainty in the analysis technique. This will be mentioned more in detail in section 5.8. SG-2 has a lower crystal area in the upper region than SG-1 and SG-3, but higher area in the central and lower region.

The degree of stirring in the melt that was performed in SG experiments goes from no stirring in SG-1, moderate stirring in SG-2 and extensive stirring in SG-3. It should however not have an effect on the crystal growth as the stirring was performed prior to the solidification. The temperature are held around 30°C above the liquidus temperature for all samples while the stirring was performed, meaning that the nucleation should not have started at this point.

The position of the cross-section can have much to say for the crystal area if the silicon has a plate-like structure. The longest crystal in experiment DS-1 is 14,2 mm. For this particular case it can be assumed that the silicon plate are cut right through, so that the entire cross-section of the silicon plate are analysed. For another cross-section it might be that this plate barely are touched, which gives a poor crystal area considering the actual size of the crystal. If the primary crystals were randomly distributed in the material, this would not affect the analysis. As it is believed that there are more crystals in the central part of the melt, the position of the cross-section are important for the results.

With the above considerations it can be concluded that the position of the cross-section are of great importance when analysing the crystal area if it is assumed that there are more Si crystals in the central part of the melt. The seed added to the melt in SG experiments was found not to increase the growth of the silicon crystals.

5.4.6 Length of primary Si crystals

Most of the silicon crystals were found to have a rod-like shape in the cross-section, which is why the crystal length was selected to give a clearer picture on the size of the crystals. The crystal length and number of crystals were found in the entire cross section area and presented in Figure 4.2 and 4.3 for all directional solidification experiments with Al-Si.

The total number of crystals can be seen from Figure 5.6. DS-3 has the highest crystal number while DS-1 has the lowest. This is consistent with the results from the crystal area analysis where DS-1 has the lowest and DS-3 has the highest value. The total number of crystals does not vary much for the SG experiments.

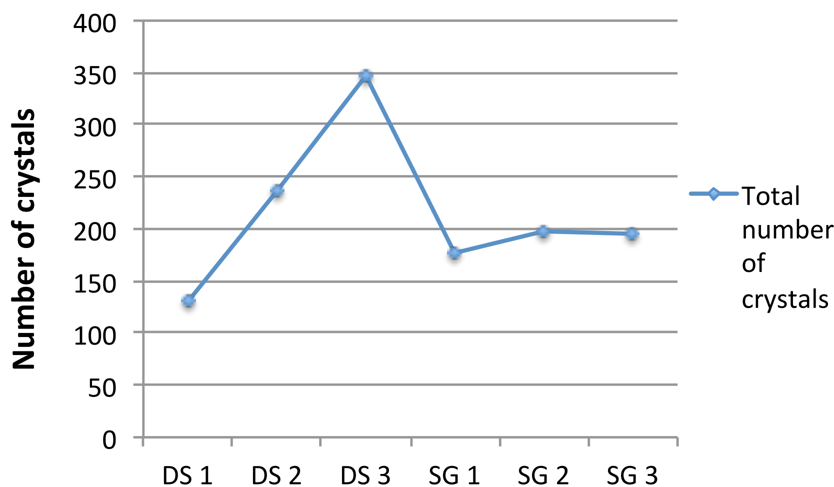

Figure 5.6, Total number of crystals found in cross-section for DS and SG experiments.

Number of crystals that has a size larger than 1 cm is presented in Figure 5.7. DS-1, which has lower silicon content than the other samples has more crystals above this size. Ullah and Carlberg [9] reported that the primary crystals should have a smaller size with a decrease in the silicon content. The length of the Si crystals found in sample DS-1 is therefor not consistent with the theory as this sample has more crystals of larger size compared to the other experiments. DS-3 on the other hand has no crystals with the size of 1 cm or larger. This is not in accordance with the literature where it is stated that the size of the crystals will increase as the solidification velocity decreases, i.e. when the pulling rate decreases. [20]

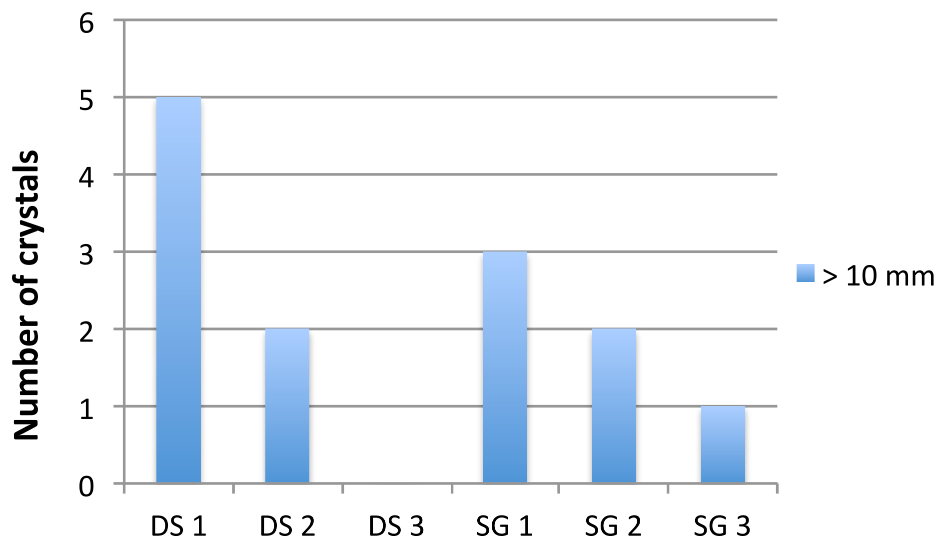

Figure 5.7, Number of crystals with size larger than 1 cm in DS and SG experiments.

The SG experiments have a decrease in number of crystals larger than 1 cm as the stirring intensity increases. However, it is believed that the stirring does not affect the crystal growth and cannot be used to describe this decline.

It is important to mention that as there are no parallels conducted in these experiments, the number of crystals larger than 1 cm can vary greatly since it applies only for a small number of crystals and are largely affected by the position of the cross-section.

5.5 Seeded growth

It was expected that the SG experiments would have seeded growth that should give a higher Si crystal area than the DS experiments. It was evident from the samples cross-section that the silicon crystals did not grow from the seed in experiment SG-1. It was believed that an oxide layer had formed between melt and seed and prevented contact between the two phases. Stirring was introduced to remove this oxide layer. First, moderate stirring was included in SG-2. No increase in the crystal growth was observed and another attempt was made to remove the oxide layer with extensive stirring in SG-3. Still no significant increase in the crystal growth was observed.

After the experiments, the upper part of the seed was stuck in the melt. The seed did have a smaller diameter than the melt, and in SG-1 it was observed that no melt had filled this cavity. After the stirring was introduced this cavity was filled, indicating that the oxide layer was removed.

The lower part of the seed was separated from the rest in SG-2 and SG-3. It was believed that it was the tension between the melted and the solid part, which made the seed to burst. During the experiments, the lower part of the seed was kept solid, ensuring that the silicon crystals would have a seed with a specific orientation to grow on. The mass of melted seed was calculated to 6g for experiment SG-2 and 6,5g for SG-3. This means that the solid seed separated from the rest of the sample should be 9,7g and 7,2 g for SG-2 and SG-3, respectively, at 960°C. The separated seed was weighed to be 8,7g for SG-2 and 7,9g for SG-3. The temperature is believed not to be exactly 960°C as the temperature gradient in the furnace are high, which means that the weight of the seed corresponds well theoretically and experimentally. Thus, it is concluded that it was the tension between liquid and solid material that caused the seed to burst. This also means that some of the seed were solid during the experiment, and was not the reason for the lack of growth on the seed.

The seed bursted only partially in SG-1, which indicates that the oxide layer prevented the seed and the Al-Si to melt together. Thus, the stirring in SG-2 and SG-3 was believed to effectively remove the oxide film at the interface.

According to the literature, a crystal is grown from the seed if the crystal and the seed have the same orientation. [27] SGS only contains silicon and a single crystal was successfully grown from the seed as the crystal orientation of the silicon had a <001> direction, same as the seed. There are some areas in the single crystal that are not completely red, which can be seen from Figure 4.9. However, it was shown that the silicon grew into one single crystal from the seed (Figure 4.8) so the small deviation from red colour is expected to be caused by small orientation differences. This indicates that it was the aluminium oxide that prevented growth from the seed in experiment SG-1. However, as the oxide layer is believed to be removed in SG-2 and SG-3 it might be other reasons why the silicon crystals could not grow from the seed.

5.6 EPMA analyses

To investigate whether the mono-Si was contaminated with aluminium and caused the silicon crystal not to grow on the seed, EPMA analysis was conducted. Figure 4.5 shows the results from the EPMA. The analysis in mono-Si area revealed that the material only contained silicon as no other elements were found, including aluminium. It was analysed on two samples from each experiment and the average are plotted in Figure 5.8. The silicon content ranged from 97,5% to 100,1%. As no other elements are found, it indicates that the silicon content was 100%. The deviation from 100% might be caused by difference in distance for the sample and the reference material, which is also why the results can exceed 100%. Thus, it was concluded that the mono-Si seed was not contaminated and was believed not to prevent growth of silicon crystals.

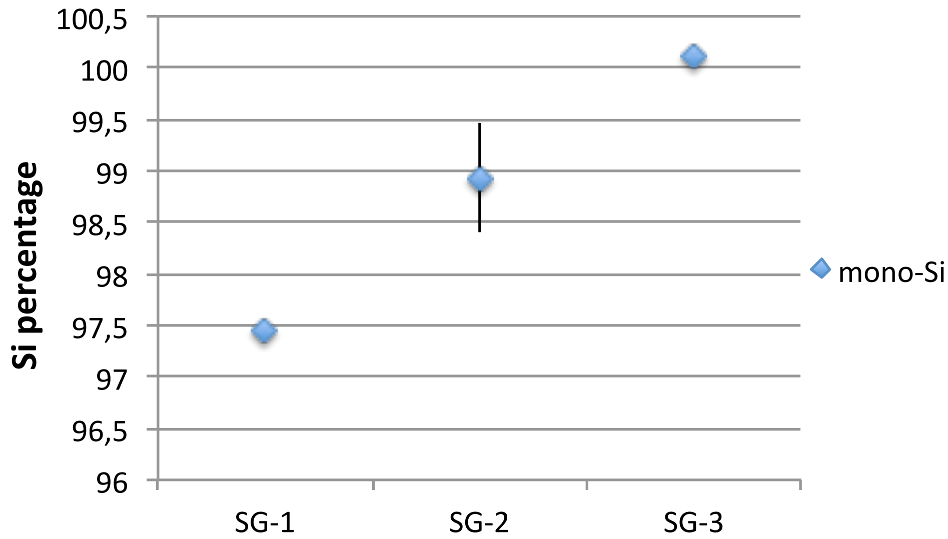

Figure 5.8, Average values of silicon percentage in mono-Si. The error bars indicate the positive and negative deviations in silicon content.

The purity of the silicon crystals was also found by EPMA in two positions of the melt for SG samples. Position 1 is nearby the interface melt-seed and position 2 is about 1 cm above the interface. Together with silicon, aluminium and iron was detected. However, the iron content was under the detection limit and could be neglected. The average values of the two samples from each experiment are shown for the two positions for Si in Figure 5.9 and for Al in Figure 5.10.

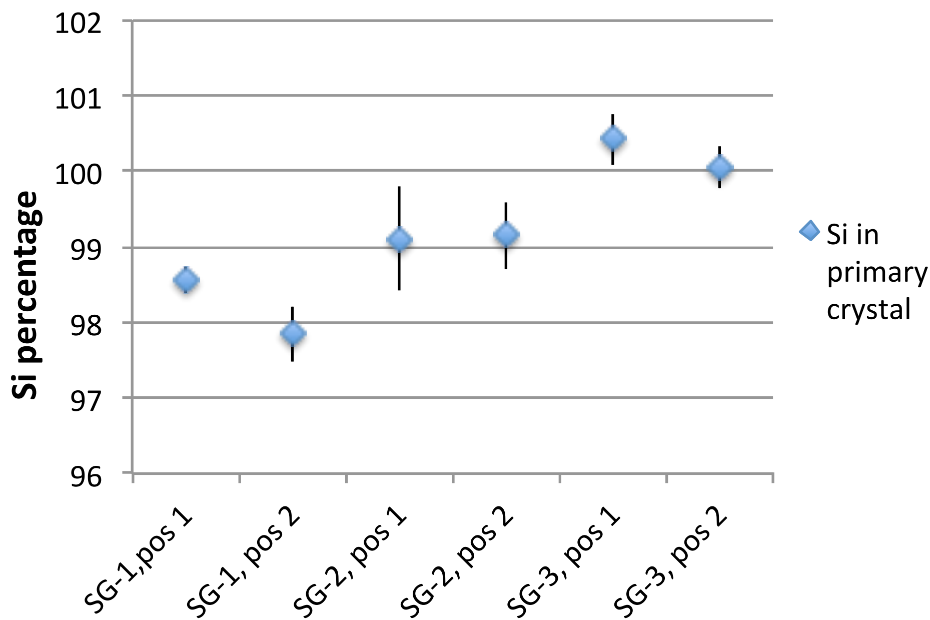

Figure 5.9, Average values of Si percentage in primary Si crystals. The error bars indicate the positive and negative deviations in silicon content.

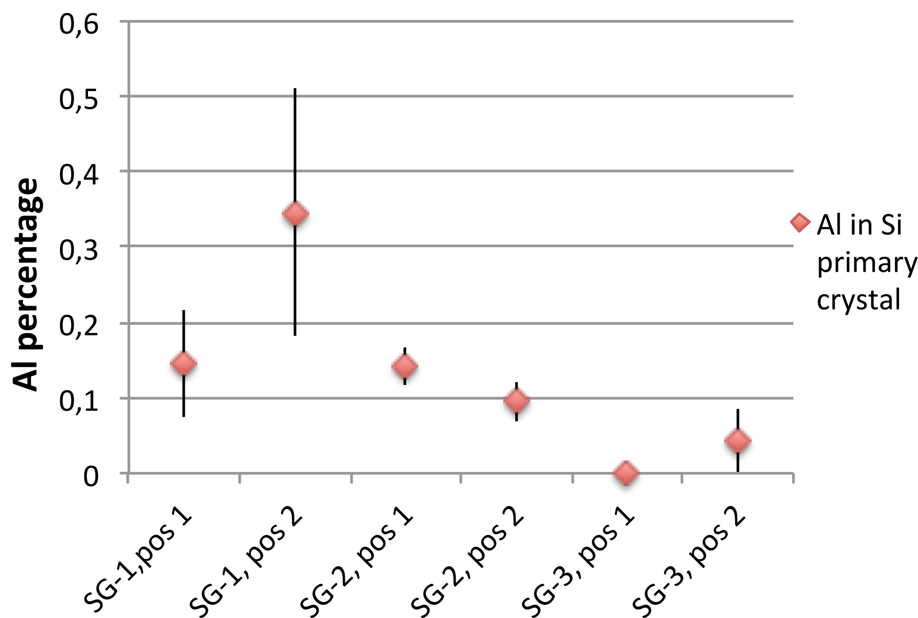

Figure 5.10, Average values of Al percentage in primary Si crystals. The error bars indicate the positive and negative deviations in aluminium content.

SG-1 has the lowest silicon content and highest aluminium content, while SG-3 has the highest silicon content and lowest aluminium content. It should be emphasized that the silicon content probably are higher due to differences in distance between sample and reference material as the sum of aluminium and silicon content does not add up to 100%.

Different values on the maximum solubility of Al in Si are reported in the literature. Yoshikawa and Morita found a maximum solubility at 1170°C of 430ppm, [10] whereas Murray and McAlister found a maximum solubility at 1190°C of 0,016±0,003at%. [11] Except from SG-3 in position 1, the aluminium content is higher than the maximum solubility. This indicates that aluminium inclusions may be present in the primary Si crystal, which is reported for primary Si crystals with plate-like growth. [9]

The reference material used to find the Al content in the EPMA contained pure Al. The accelerating voltage used to analyse the elements can penetrate deeper than the Si crystal, meaning that the EPMA would analyse on the material below the crystal as well. This must be mentioned as it can cause error in the results.

5.7 Electromagnetic separation

In an induction furnace, when current pass through the induction coil, a magnetic field is created. It was expected from the theory that the silicon crystals would be captured by the magnetic field, separating the silicon crystals from the Al-Si melt. Silicon crystals separated from the melt are done by Yoshikawa and Morita [22] and shown in Figure 5.11a.

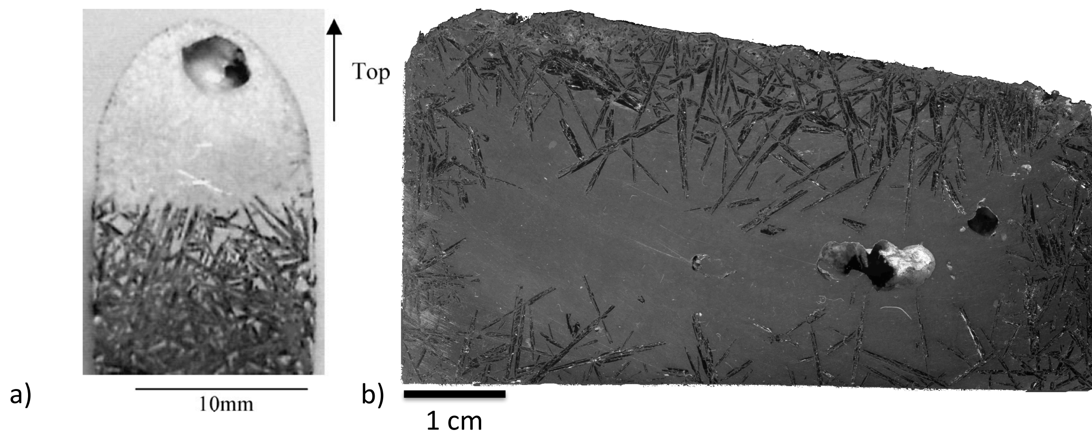

Figure 5.11, a) Silicon crystals agglomerated to the lower part of the melt by electromagnetic force b) Silicon crystals in cross-section for IH experiment.

All the silicon crystals are agglomerated in the lower part of the melt. Their sample was positioned below the induction coil, while IH sample was positioned in the induction coil. It was expected that this would cause the Si crystals to agglomerate in the vicinity of the crucible wall and not in the lower part of the melt as was the case in Figure 5.11a. Scanned image of the cross-section of sample IH is shown in Figure 5.11b. The image shows that some crystals are positioned near the crucible wall while the major part is gathered in the top of the melt. This is not as expected as the major part of the crystals should be at the vicinity of the crucible wall. Yoshikawa and co-workers combined the electromagnetic force with directional solidification. The diameter of the sample are also smaller than what was used in IH experiment, and can partly explain the differences in Si crystal separation from melt.

When IH experiment was conducted an apparent layer of oxides formed at the top of the melt. The oxide layer would disturb the velocity flow pattern shown in Figure 2.19, which is caused by the magnetic field. The oxide layer appears as a slag phase in the top of the melt and makes the flow in the melt to move faster, which can explain the more random position of Si crystals.

The top area has 59% of all the crystals in the sample, while the bottom area has 9%. This could imply that the gravity force has had an influence on the crystals, since they have a lower density than the melt and are expected to float. However, Equation 2.24 shows that when electromagnetic forces are present, they take the place of the gravity force. Thus, gravity force is not likely to explain the gathering of Si crystals in the top of the melt and the oxide layer is believed to be the cause.

The crystal area from top, bottom, right and left is presented in Figure 4.7. The crystals in the right and left area, respectively, are 13% and 19% of crystals from the entire sample. As this is the same area in the sample, the maximum uncertainty is found to ±3% from these values.

The analysis of the entire sample gave a Si crystal area of 32%. The theoretical maximum crystal area is calculated to 25,63wt% when the alloy contains 35wt%Si. As the material analysis show an uneven distribution of silicon it might be also here, that the material used in the experiment contained more than 35wt%Si. It must also be emphasized that the analysis are conducted on a scanned image, as the sample size were too large to be captured with a light microscope. The low magnification may affect the accuracy.

5.8 Analysing technique

ImageAccess EasyLab is used to find the crystal area. The program requires good contrast between the primary Si crystals and the eutectic phase to separate them from each other. The grey coloured Si crystals have some black areas as well, caused from sample preparation as it made some parts of the crystal to crack. Since the crystals are both grey and black and not easy to separate from the

eutectic phase they are coloured with a different colour than the eutectic phase. The Si crystals appear as rods in the cross-section but the shape of the rods are various and make the colouring difficult. This can cause error in the analysing results as the detected Si crystals area in the cross-section can vary from the reality.

When the length of the Si crystal is found, a line is drawn along the crystal in the ImageAccess EasyLab program. Some of the smaller crystals have different shapes and are not necessary shaped as rods. In these cases it is not always easy to distinguish between length and width, but the longest length possible is consistently measured in all samples.

In many places on the samples it appears that some crystals are longer than what is shown in the given cross-section. Figure 5.12 shows an example of this, which is a microscope image taken from experiment DS-1. The red circles show the areas where it is believed that the crystals shown on each side of the other crystal are one crystal in another cross-section plane, because of the similar shape. Thus, it is important to emphasize that the length of the silicon crystals in the samples are found by the cross-section and is not applicable for the whole sample.

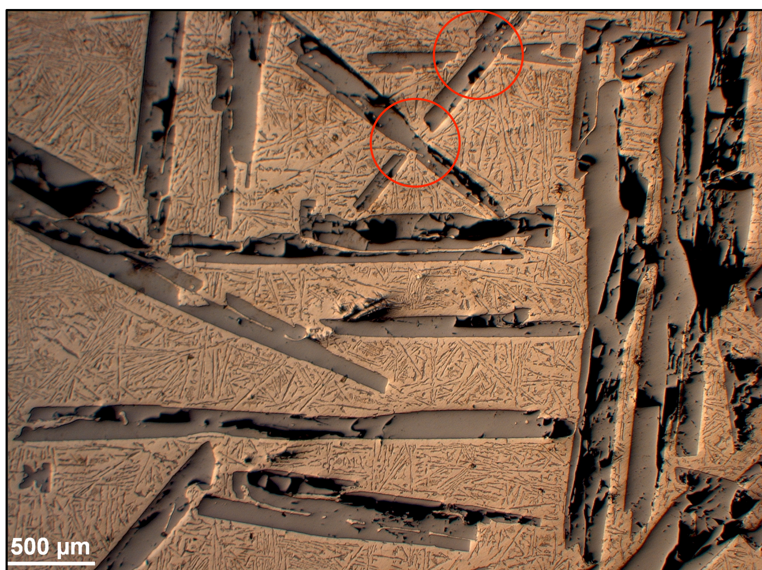

Figure 5.12, Microscope image with 2,5X magnification taken from DS-1, which shows an example of silicon crystals in the cross-section.

6 Conclusion

Solvent refining with Al-Si melt is used to obtain refined primary Si crystals. Agglomeration of silicon crystals in an Al-Si melt and larger sized crystals during crystallisation could simplify the following leaching process, which is necessary to collect the Si crystals. Obtaining Si crystals with a larger size can be beneficial for the Clean Silicon process as acid amount can be reduced, which has a positive influence on the economy and environment if the process is to be industrialised.

The critical crystal growth is found for samples with directionally solidified 35wt%Si material. The crystal growth is slow and therefor bulk Si growth is unrealistic for an actual refining process with Al-Si melt. It is concluded that acid leaching is necessary to collect the Si crystals from the material.

The findings on agglomeration and size of silicon crystals are;

- Al-35wt%Si material and pulling rate of 0,18mm/min during directional solidification was found to be the most appropriate parameters of the ones conducted
- Primary Si crystals are not found exclusively in one part of the Al-Si melt for directional solidification method
- Primary Si crystals are not found exclusively in one part of the Al-Si melt for electromagnetic force method
- Mono-crystalline Si seed added to the melt did not improve Si crystal growth
- The size of the Si crystals found in directionally solidified material are small compared to findings reported in the literature
- Si single crystal was grown from mono-crystalline Si seed from silicon material during directional solidification

Agglomeration of Si primary crystals is not successful in either method. The attempts to increase the Si crystal size were not successful. The pulling rate and temperature gradient during directional solidification are too high and caused

the weak crystal growth and nearly uniform Si crystal distribution in these experiments. The oxide layer caused the unsuccessful agglomeration during induction heating.

7 Further work

Directional solidification as solidification method can be used further to find the appropriate growth conditions for Si crystals by varying pulling rate and temperature gradient. A slower pulling rate and lower temperature gradient can be investigated, as it is expected to give higher Si crystal growth. If the crystal growth rate can be successfully controlled, the Al content of the Si crystals could be decreased to the level of solid solubility.

Growth of Si crystals on mono-crystalline Si seed can be investigated further. If it is found to be successful, it could be interesting to investigate the Si crystal growth by pulling the sample upwards, as Si crystals are expected to float. Also, smaller seeds could be added to the melt to increase the potential growth surface.

Electromagnetic separation could be conducted with pure material and good vacuum excluding the possibility of oxide formation. Position of the sample could be in the induction coil or below the induction coil, and it could be combined with directional solidification.

Clean Silicon AS has developed a process where solvent refining with Al-Si melt is used to achieve the purity of SoG-Si. If larger sized Si crystals can be grown it could make the acid leaching step more effective, which is why this work is of importance.

References

1. Lee, W., et al., *Metal impurities behaviors of silicon in the fractional melting process.* Solar Energy Materials and Solar Cells, 2011. **95**(1): p. 59-62.
2. Swanson, R.M. *Developments in silicon solar cells*. 2007. IEEE.
3. Istratov, A., et al., *Control of metal impurities in "dirty" multicrystalline silicon for solar cells.* Materials Science and Engineering: B, 2006. **134**(2): p. 282-286.
4. Woditsch, P. and W. Koch, *Solar grade silicon feedstock supply for PV industry.* Solar Energy Materials and Solar Cells, 2002. **72**(1): p. 11-26.
5. Braga, A., et al., *New processes for the production of solar-grade polycrystalline silicon: A review.* Solar Energy Materials and Solar Cells, 2008. **92**(4): p. 418-424.
6. Tathgar, H. *Refining by solvent refining*. in *Upgraded metallurgical grade silicon*. 2012. Norway.
7. Nishi, Y., Y. Kang, and K. Morita, *Control of Si Crystal Growth during Solidification of Si-Al Melt.* Materials transactions, 2010. **51**(7): p. 1227-1230.
8. Zhao, L.X., et al., *Low-temperature purification process of metallurgical silicon.* Transactions of Nonferrous Metals Society of China, 2011. **21**(5): p. 1185-1192.
9. Ullah, M.W. and T. Carlberg, *Silicon crystal morphologies during solidification refining from Al–Si melts.* Journal of crystal growth, 2011. **318**(1): p. 212-218.
10. Yoshikawa, T. and K. Morita, *Solid solubilities and thermodynamic properties of aluminum in solid silicon.* Journal of the Electrochemical Society, 2003. **150**: p. G465-G468.
11. Murray, J. and A. McAlister, *The Al-Si (aluminum-silicon) system.* Journal of Phase Equilibria, 1984. **5**(1): p. 74-84.
12. Halm, A., et al., *Large area industrial solar cells on low cost 100% Mc SoG Si substrates: Efficiencies exceeding 16%.* Proceedings of the 35th IEEE PVSEC Honolulu, USA, 2010.
13. Mullin, J.W., *Crystallization*. 3 ed1993: A Butterworth-Heinemann Title.

14. Fisher, K. and W. Kurz, *Fundamentals of solidification*. 4 ed1998, Switzerland: Trans Tech Publications Ltd.
15. Stefanescu, D.M., *Science and engineering of casting solidification*2002, New York: Kluwer Academic / Plenum Publishers.
16. Flemings, M.C., *Solidification processing*1974: McGraw-HillInc.
17. Porter, D.A. and K.E. Easterling, *Phase transformations in metals and alloys*. 2 ed1992, London: Chapman & Hall.
18. Myerson, A.S., *Handbook of industrial crystallization*1993: Butterworth-Heinemann.
19. Lu, S.Z. and A. Hellawell, *Growth mechanisms of silicon in Al-Si alloys.* Journal of crystal growth, 1985. **73**(2): p. 316-328.
20. Miyahara, H., et al., *Effect of twin growth on unidirectional solidification control of multicrystal silicon for solar cells.* Materials transactions, 2005. **46**(5): p. 935-943.
21. Gumaste, J., et al., *Solvent refining of metallurgical grade silicon.* Solar Energy Materials, 1987. **16**(4): p. 289-296.
22. Yoshikawa, T. and K. Morita, *Refining of Si by the solidification of Si-Al melt with electromagnetic force.* ISIJ international, 2005. **45**(7): p. 967-971.
23. Kvande, R., *Incorporation of Impurities during Directional Solidification of Multicrystalline Silicon for Solar Cells.* Department of Materials Science and Engineering, NTNU: Trondheim, Norway, 2008.
24. Ciftja, A., *Solar silicon refining, Inclusions, settling, filtration, wetting.* LAP Lambert Academic Publishing, New York, 2010.
25. Kou, S., *Transport phenomena and materials processing*1996, Canada: John Wiley & Sons, Inc.
26. Koch, W., et al., *Handbook of photovoltaic science and engineering*2003, England: John Wiley & Sons, Ltd.
27. Fujiwara, K., et al., *Grain growth behaviors of polycrystalline silicon during melt growth processes.* Journal of crystal growth, 2004. **266**(4): p. 441-448.
28. Morita, K. and T. Miki, *Thermodynamics of solar-grade-silicon refining.* Intermetallics, 2003. **11**(11): p. 1111-1117.

29. *Al-Si binary phase diagram*. 2011 14.10.2011]; Available from: http://www.globalsino.com/micro/1/images/1micro9989.gif.
30. Morita, K. and T. Yoshikawa, *Thermodynamic evaluation of new metallurgical refining processes for SOG-silicon production.* Transactions of Nonferrous Metals Society of China, 2011. **21**(3): p. 685-690.
31. Trumbore, F., *Solid solubilities of impurity elements in germanium and silicon.* Bell Syst. Tech. J, 1960. **39**(1): p. 205.
32. Yoshikawa, T. and K. Morita, *Refining of silicon during its solidification from a Si-Al melt.* Journal of crystal growth, 2009. **311**(3): p. 776-779.
33. Yoshikawa, T. and K. Morita, *Removal of B from Si by solidification refining with Si-Al melts.* Metallurgical and Materials Transactions B, 2005. **36**(6): p. 731-736.
34. Yoshikawa, T. and K. Morita, *Removal of phosphorus by the solidification refining with Si-Al melts.* Science and Technology of Advanced Materials, 2003. **4**(6): p. 531-537.
35. Fredriksson, H. and U. Åkerlind, *Materials processing during casting*2006: John Wiley & Sons Inc.
36. Mjøs, Ø., *Directional solidification of silicon for solar cells.* Department of Materials Science and Engineering, NTNU: Trondheim, Norway, 2006.
37. Dawless, R., et al., *Production of extreme-purity aluminum and silicon by fractional crystallization processing.* Journal of crystal growth, 1988. **89**(1): p. 68-74.
38. Liu, Y., et al., *Research on Removal of Boron from Metallurgical Grade Silicon by Si-Al Alloying.* Advanced Materials Research, 2011. **156**: p. 1037-1040.
39. Kadkhodabeigi, M., et al., *Removal of Silicon carbide (SiC) Particles from Solar Grade Silicon Melts by Imposition of High Frequency Magnetic Field*.
40. Shu, D., et al., *Study of electromagnetic separation of nometallic inclusions from aluminum melt.* Metallurgical and Materials Transactions A, 1999. **30**(11): p. 2979-2988.
41. Motzfeldt, K., *Basic design of laboratory furnaces*, 2004, Institutt for materialteknologi, NTNU: Trondheim.

42. Forwald, K.R., *Properties of some silicon rich alloys.* Metallurgical institute, NTNU, Trondheim, Norway, 1997.
43. Maitland, T. and S. Sitzman, *Electron backscatter diffraction (EBSD) technique and materials characterization examples.* Scanning Microscopy for Nanotechnology Techniques and Applications, 2007: p. 41-75.

Appendix 1

Material analyses Al-18,5wt%Si

Table A1.1, Analysis of Al-18,5wt%Si master alloy provided by Clean Silicon AS.

Element	Content (wt%)
Si	18,53
Fe	0,17
Ti	0,012
Mn	0,009
Mg	0,004
Ni	0,004
Zn	0,002
Sn	0,002
P	0,0019
Zr	0,001
Ca	0,0002
Na	0
Pb	0

Table A1.1 show the silicon content together with the content of trace elements for Al-18,5wt%Si.

Appendix 2

Material analysis Al-35wt%Si

Table A2.1, Analysis of Al-35wt%Si master alloy by XRF.

Element	Content (wt%)
Si	46,1
Al	53,4

Table A2.1 show the content of Al and Si for Al-35wt%Si.

Table A2.2, Analysis of trace elements in Al-35wt%Si master alloy by ICP-MS.

Element	Content (ppm)
Fe	3931,27
Ga	102,20
Zn	66,81
Ti	54,29
Ca	39,10
Mn	36,46
Bi	32,21
Ni	25,08
Na	19,03
Mg	18,13
Cu	12,88
B	9,05
Pb	7,76
P	7,15
Zr	2,37
Sn	1,39

Two parallels of eight analysis points cut out from different positions in the master alloy were analysed. The average of impurity concentration from the eight points is presented in Table A2.2. Figure A2.1 show at which position the analysed material were taken from the master alloy. More in depth analyse results are shown by the graphs in Figure A2.2.

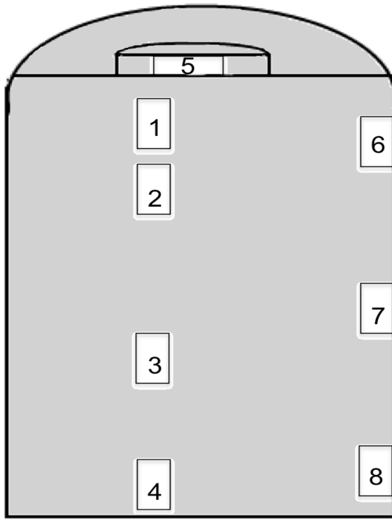

Figure A2.1, Selected positions of analysed material from the master alloy.

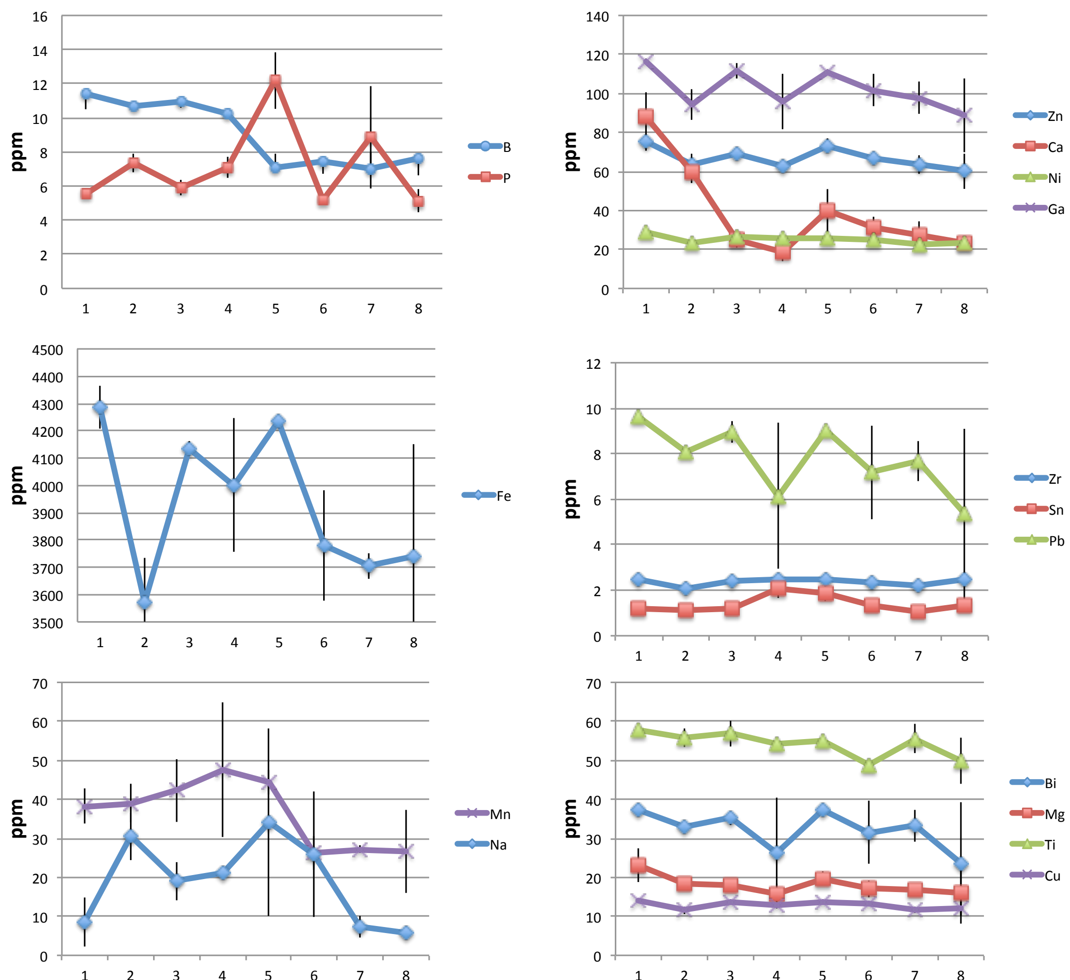

Figure A2.2, Analysis of trace elements for selected points in the alloy material shown by Figure A2.1. Note the varying ppm values for the different graphs.

Appendix 3

Light microscope images of DS-1

Figure A3.1, Several light microscopy images with 2,5X magnification put together to form the whole cross-section of DS-1.